Monolayer FeSe on $SrTiO_3$

Dennis Huang[1] and Jennifer E. Hoffman[1,2]

[1]Department of Physics, Harvard University, Cambridge, Massachusetts 02138; email: dhuang@physics.harvard.edu, jhoffman@physics.harvard.edu

[2]Department of Physics & Astronomy, University of British Columbia, Vancouver, British Columbia V6T 1Z1, Canada

Annu. Rev. Condens. Matter Phys. 2017. 8:311–36

First published online as a Review in Advance on February 23, 2017

The *Annual Review of Condensed Matter Physics* is online at conmatphys.annualreviews.org

https://doi.org/10.1146/annurev-conmatphys-031016-025242

Keywords

superconductivity, iron pnictides and chalcogenides, oxides, thin-film interfaces

Abstract

Epitaxial engineering of solid state heterointerfaces is a leading avenue to realizing enhanced or novel electronic states of matter. As a recent example, bulk FeSe is an unconventional superconductor with a modest transition temperature (T_c) of 9 K. However, when a single atomic layer of FeSe is grown on $SrTiO_3$, its T_c can skyrocket by an order of magnitude to 65 K or 109 K. Since this discovery in 2012, efforts to reproduce, understand, and extend these findings continue to draw both excitement and scrutiny. In this review, we first present a critical survey of experimental measurements performed using a wide range of techniques. We then turn to the open question of microscopic mechanisms of superconductivity. We examine contrasting indications for both phononic (conventional) and magnetic/orbital (unconventional) means of electron pairing, as well as speculations about whether they could work cooperatively to boost T_c in a monolayer of FeSe.

1. INTRODUCTION

Interface engineering lies at the vanguard of current research in condensed matter physics and novel materials. From a fundamental perspective, quantum-size and electron correlation effects are enhanced in reduced dimensionality, often resulting in unexpected phenomena. From a technological perspective, as the pace of electronics miniaturization fast approaches the limit of conventional semiconductors, alternative paradigms, such as atomically thin materials and interfaces with manifestly quantum behavior, are needed to assume the mantle of next-generation electronics. With improving ability to assemble atomically sharp interfaces "bottom up" through molecular beam epitaxy (MBE) or mechanical stacking of 2D-layered materials, many possibilities abound.

As the central example of this review, interface engineering holds promise in tuning, boosting, or generating superconducting states of matter—low-temperature quantum phases in which electrons form Cooper pairs and charge transport is lossless. Since its discovery in 1911, superconductivity has continued to fascinate and baffle condensed matter physicists, and the goal of realizing room-temperature superconductivity has remained elusive. Within the past decade, various examples of interface superconductivity have been observed. When two insulating oxides, $LaAlO_3$ and $SrTiO_3$, are put together, a superconducting electron gas is formed at the interface, albeit with a low transition temperature (T_c) of 200 mK (1). When a bilayer of insulating La_2CuO_4 and metallic $La_{1.55}Sr_{0.45}CuO_4$ is formed, the aggregate system displays a T_c exceeding 50 K (2). And as the latest example, when a single–unit cell (1UC) layer of FeSe is deposited on $SrTiO_3$ (3), its T_c skyrockets up to 65 K (4–7) or 109 K (8), which is an order of magnitude above its bulk T_c of 9 K. In this review, we cover key experimental and theoretical developments related to 1UC FeSe/$SrTiO_3$ up to early 2016. We focus on measurements of basic properties and questions of superconducting mechanisms.

1.1. Approaching the Two-Dimensional Limit with FeSe

FeSe possesses the simplest structure among the iron-based superconductors, consisting of superconducting Se–Fe–Se triple layers stacked by van der Waals forces with no buffer layers (9). **Figure 1*a*** shows the structure of one triple layer, which includes Fe atoms arranged in a square lattice and Se atoms staggered above and below the Fe plane. Due to the staggering, the

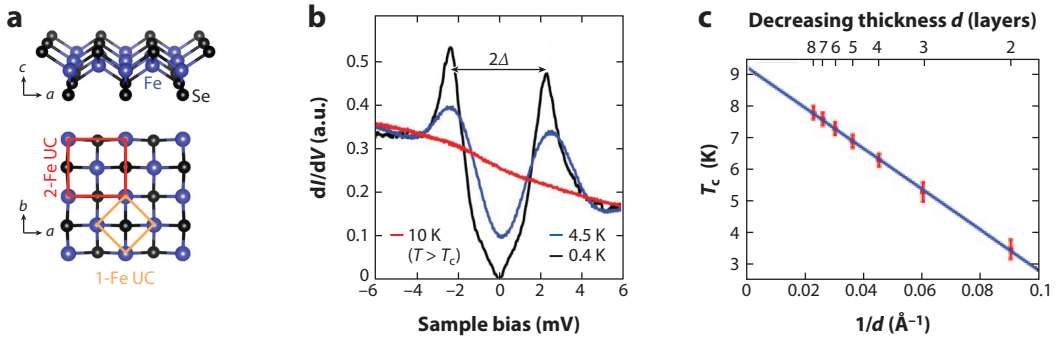

Figure 1

(*a*) Crystal structure of an FeSe monolayer; side and top views. The orange and red boxes enclose the 1-Fe unit cell (UC) and 2-Fe UC, respectively. (*b*) Scanning tunneling microscopy dI/dV spectra of multilayer FeSe/SiC, exhibiting a V-shaped superconducting gap of $\Delta = 2.2$ meV at $T = 0.4$ K, which disappears above 10 K. Adapted from Reference 11, their figure 1, with permission. (*c*) Gap-closing temperature, T_c, of multilayer FeSe/SiC as a function of inverse FeSe thickness, $1/d$. Adapted from Reference 12, their figure 5, with permission.

primitive UC contains two Fe atoms (and two Se atoms). However, because the low-energy bands of FeSe are dominated by Fe 3*d* orbitals, many theories or spectroscopies reference the 1-Fe UC for convenience.

By virtue of its structural simplicity, FeSe should be the prototypical iron-based superconductor to investigate, except it proved difficult to synthesize in high quality at first. Its superconducting polymorph occupies a narrow region in the Fe–Se alloy phase diagram (10), complicating common melt and self-flux growths. In 2011, Song et al. (11, 12) used MBE to grow pristine FeSe films on graphitized SiC. Using scanning tunneling microscopy (STM), they resolved clean surfaces with only one atomic defect per 70,000 Se sites. Measurements of tunneling conductance ($\mathrm{d}I/\mathrm{d}V$), which is proportional to the local density of states, revealed two signatures of a superconducting state: (*a*) a V-shaped gap of $\Delta = 2.2$ meV, representing the binding energy of paired electrons, that disappeared above 10 K (**Figure 1*b***); and (*b*) vortices in the presence of a perpendicular magnetic field. Although MBE-grown films are not amenable to many bulk and thermodynamic probes, they have other advantages. Both the monolayer limit and interface interactions with different substrates can be readily examined.

Song et al. found that the FeSe films interacted weakly with the graphitized SiC substrate (islands could be displaced by an STM tip) and were thereby close to the free-standing limit (12). Upon decreasing film thickness, T_c, as measured by the gap-closing temperature, dropped from 7.8 K (8UC-thick FeSe) to below 2.2 K (1UC-thick FeSe), the base temperature of their experiment (**Figure 1*c***). The drop exhibited a $1 - d_c/d$ dependence, d being the film thickness and d_c being a critical value. This thin-film behavior was explained long ago as resulting from a general, surface boundary condition with the Ginzburg–Landau equation (13). Thus in 2011, the 2D limit of FeSe did not appear to be a promising regime to explore, unless new microscopic effects could be introduced.

1.2. Monolayer FeSe Gets an Oxide Boost

It came as a great surprise a year later that monolayer FeSe could undergo an order-of-magnitude T_c enhancement when grown epitaxially on $SrTiO_3$ (001). The lattice mismatch between bulk FeSe [$a = 3.77$ Å (14)] and $SrTiO_3$ [$a = 3.905$ Å (15)] is roughly 3%. STM measurements by Wang et al. (3) revealed a topographic period-doubling (**Figure 2*a***) and a large U-shaped, double-gap structure (9.0 meV and 20.1 meV) in 1UC FeSe/$SrTiO_3$ (**Figure 2*b***), with closing temperature T_c above their experimental limit of 42.9 K. Intriguingly, this superconductivity boost did not persist or even proximitize low-T_c superconductivity in a second UC of FeSe deposited on the heterostructure. STM $\mathrm{d}I/\mathrm{d}V$ measurements, whose probing depth is likely limited to the surface FeSe layer, instead showed a semiconducting spectrum on the second FeSe layer (**Figure 2*c***). This observation points to an underlying interface effect, one that is atomically localized to the first UC of FeSe on $SrTiO_3$. Wang et al. speculated that electron–phonon coupling could be enhanced at the interface and boost T_c, based on their previous work with Pb/Si (111) and In/Si (111) films (16).

Due to technical challenges, Wang et al. (3) could measure transport only in a Si-capped, 5UC FeSe/$SrTiO_3$ heterostructure. They measured zero resistance at some temperature lower than 30 K and extrapolated a resistive onset temperature around 53 K. (As shown by STM spectroscopy in **Figure 2*b,c***, the superconducting signal originates from the interface FeSe layer only.)

Angle-resolved photoemission spectroscopy (ARPES) measurements in the same year provided initial insights into the role of the interface. ARPES can map filled-state band structure in momentum space. Liu et al. (17) found that the Fermi surface (FS) of 1UC FeSe/$SrTiO_3$ comprises nearly circular electron pockets at the Brillouin zone (BZ) corner M (**Figure 2*d,e***). In contrast to bulk FeSe (18–21), where additional hole FSs exist at the zone center Γ, here the corresponding

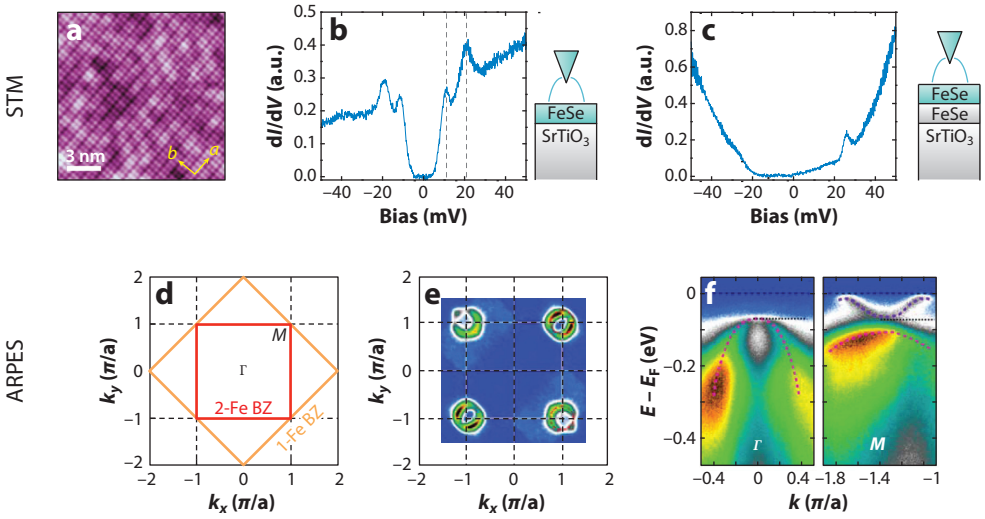

Figure 2

(*a–c*) Initial scanning tunneling microscopy (STM) measurements of 1–unit cell (UC) FeSe/$SrTiO_3$. Adapted from Reference 3, their figure 1, with permission. (*a*) Atomically resolved topography. Each bright spot represents a top-layer Se atom. (*b*,*c*) Contrasting dI/dV spectra of 1UC (superconducting) and 2UC (nonsuperconducting) FeSe/$SrTiO_3$. The dashed vertical lines in panel *b* mark two gap edge peaks at 9 mV and 20.1 mV. The schematics illustrate that the tunneling depth is largely restricted to the surface FeSe layer, so it is not possible to determine from panel *c* alone whether the presence of the second UC has altered the high-T_c superconductivity in the first UC. (*d–f*) Initial angle-resolved photoemission spectroscopy (ARPES) measurements of 1UC FeSe/$SrTiO_3$. Adapted from Reference 17 with permission. (*d*) Brillouin zone (BZ) conventions. (*e*) Fermi surface (FS) map revealing electron pockets at the BZ corner M (as shown in panel *d*) and the overall electron-doped nature of 1UC FeSe/$SrTiO_3$. Adapted from Reference 17, their figure 1, with permission. (*f*) High-symmetry cuts across the BZ center Γ and corner M, revealing additional occupied bands. Adapted from Reference 17, their figures 1 and 2, with permission.

hole pocket is sunken 65–80 meV below the Fermi energy (E_F) (**Figure 2*f***). Assuming doubly degenerate electron pockets, a Luttinger count yields 0.10 electrons/Fe atom. Thus, relative to its bulk, 1UC FeSe appears to be electron-doped from the substrate. To provide further support for the superconducting nature of 1UC FeSe/$SrTiO_3$, Liu et al. resolved nearly isotropic gaps on the electron pockets at each M point, of values 13 ± 2 meV and 15 ± 2 meV for two samples. They found the gap-closing temperature to be 55 ± 5 K.

Before proceeding, we reiterate that monolayer FeSe/$SrTiO_3$ is not monolayer FeSe. A giant T_c enhancement is present only in the former, due to some effect introduced by the $SrTiO_3$.

2. EXPERIMENTAL CHALLENGES

A foremost challenge related to 1UC FeSe/$SrTiO_3$ has been the characterization of its growth, atomic structure, and superconducting metrics. As a point of emphasis, bulk probes are not effective for this system. Not only is the cross section of a single UC layer minuscule but FeSe also exhibits extreme air sensitivity, hampering ex situ measurements. Thus, the basic goal of determining T_c represents a nontrivial endeavor requiring customized and integrated instrumentation in ultra-high vacuum. Example apparatuses include combined MBE-ARPES-STM systems, double chalcogen-MBE/oxide-MBE chambers, and customized in situ, four-point probes.

In this section, we review various experiments related to film characterization categorized under three questions: What is T_c? What are the necessary growth conditions? What is the interface

Table 1 Comparison of T_c measurements across different probes, heterostructures, and laboratories

Technique	Definition	Heterostructure	Value (K)	Reference
In situ				
STM	Gap-closing T	1UC FeSe/Nb:$SrTiO_3$	>42.9	3
STM	Gap-closing T	1UC FeSe/$SrTiO_3$	>50.1	23
ARPES	Gap-closing T	1UC FeSe/Nb:$SrTiO_3$	65 ± 5	4
ARPES	Gap-closing T	1UC FeSe/Nb:$SrTiO_3$	60 ± 5	5
ARPES	Gap-closing T	1UC FeSe/Nb:$SrTiO_3$/$KTaO_3$	70	24
ARPES	Gap-closing T	1UC FeSe/Nb:$BaTiO_3$/$KTaO_3$	75 ± 2	22
ARPES	Gap-closing T	1UC FeSe/Nb:$SrTiO_3$	58 ± 7	6
4-probe	Zero resistance	1UC FeSe/Nb:$SrTiO_3$	109	8
Ex situ				
Transport	Zero resistance Onset T	Si/5UC FeSe/$SrTiO_3$	<30 53	3
Transport	Zero resistance Onset T	Si/10UC FeTe/1UC FeSe/$SrTiO_3$	23.5 40.2	25
Magnetization	Onset T	Si/10UC FeTe/1UC FeSe/$SrTiO_3$	21	25
Magnetization	Onset T	Si/10UC FeTe/3–4UC FeSe/$SrTiO_3$	20–45	26
Magnetization	Onset T	10UC FeTe/1UC FeSe/Nb:$SrTiO_3$	85	27
Magnetization	Onset T	Se/2UC FeSe/2UC $Fe_{0.96}Co_{0.04}Se$/1UC FeSe/Nb:$SrTiO_3$	65	7

We distinguish measurements without (in situ) and with (ex situ) a capping layer. Abbreviations: ARPES, angle-resolved photoemission spectroscopy; STM, scanning tunneling microscopy.

structure? We attempt to reflect the sentiments of the scientific community by conveying both the excitement related to the spectacular findings of tour-de-force experiments and scrutiny related to the challenging nature of these feats and of film quality/homogeneity.

2.1. What is T_c?

Table 1 presents a comparison of T_c measurements across different probes, heterostructures, and laboratories. Among various in situ ARPES measurements (4–6), there is consensus in a gap-closing temperature $T_c \sim 65$ K. Some variation exists with the degree of postgrowth annealing (4) (see Section 2.2 for details). Enhancement of T_c up to 75 K is possible if extra tensile strain is introduced through an additional $KTaO_3$ substrate (22).

A more robust proof of superconductivity would include (*a*) a zero-resistance state and (*b*) the Meissner effect (perfect diamagnetism). Due to air sensitivity, ex situ transport and thermodynamic measurements require film capping, with amorphous Se (28), amorphous Si (3), or epitaxial FeTe (25). In all cases, film characteristics were degraded. Transport measurements of capped heterostructures have found a zero-resistance state below ~30 K, and a rough onset temperature possibly up to ~50 K. Similarly, magnetization measurements of capped samples have suffered from weak signals, broadened onset temperatures, or low superconducting volume fractions.

Given that many potential applications require some degree of atmosphere exposure, it remains crucial to investigate why capping, particularly epitaxial FeTe, has not worked well. FeTe possesses the same crystal structure as FeSe and its layers interact via van der Waals forces, so naively it should not create a severe disturbance of the FeSe layer below. Several hypotheses have been put

forward. Ultrafast spectroscopy revealed an acoustic phonon mode in FeTe that may relax phonon-mediated pairing in FeSe (29). Alternatively, cross-sectional transmission electron microscopy (TEM) revealed that intermixing with the capping layer can occur, whereby Te atoms substitute Se atoms in the FeSe monolayer (30). As a third possibility, Zhao et al. proposed that FeTe may hole-dope FeSe, reducing T_c (31).

In **Table 1**, we distinguish heterostructures that have conducting, Nb-doped $SrTiO_3$ from those that do not (undoped, bulk-insulating $SrTiO_3$). In general, transport measurements require an insulating $SrTiO_3$ substrate, but there are speculations that Nb-doped $SrTiO_3$ produces higher-quality films. Sun et al. (27) hinted that "high quality FeSe films are easier to be achieved by MBE growth on conductive $SrTiO_3$ substrates comparing to insulating $SrTiO_3$ substrates since the conductive $SrTiO_3$ substrate shows more flat and homogeneous surface for sample growth."

2.1.1. In situ, micro-four-point measurements. In late 2014, Ge et al. reported an astonishing new record T_c above 100 K in 1UC FeSe/$SrTiO_3$ (8). Here, we review their experiment in detail. The authors converted a commercial cryogenic STM into an in situ, micro-four-point probe by replacing the single STM tip with a set of four Cu/Au wires separated by 10–100 μm (**Figure 3*a***). The four probes were collectively brought toward the sample at a 20° incline using the STM positioning system until Ohmic contact with the sample was established for each probe. **Figure 3*c*** shows several four-point I–V curves, which transition from a nonlinear (superconducting, zero-resistance) to linear (normal state, Ohmic) line shape as the temperature was raised above T_c.

Due to sample inhomogeneity or film damage from probes, linear I–V curves were sometimes observed below T_c. As a result, Ge et al. (8) compiled resistance versus temperature (R–T) plots in two manners. First, they acquired four-point I–V measurements from separate locations for each temperature (**Figure 3*b***). As long as one I–V curve per temperature showed signs of zero resistance, that temperature was deemed to be below T_c. With this method, Ge et al. determined T_c to be 109 K. Alternatively, they were also able to construct R–T plots from measurements at one location, with a sequence of decreasing magnetic fields (**Figure 3*d***). With this second method, they demonstrated a similar T_c of 99 K. The magnetoresistance measurements in **Figure 3*e*** were also acquired at a fixed location.

We enumerate questions that have been raised about this experiment and the authors' responses:

1. *Question:* Is the result reproducible on multiple samples?
   Response: Ten different samples show similar results. Data from four samples are shown in the paper.
2. *Question:* Is it possible that the authors simply lost a current lead contact as the contacts cooled, resulting in a sudden drop of the measured V to zero?
   Response: No, the authors measured full I–V curves at each temperature and magnetic field (B) and extracted a T-dependent and B-dependent critical current (e.g., see **Figure 3*d*,*e***).
3. *Question:* Is it possible that the actual T of the sample is lower than the recorded T, giving the appearance of higher T_c?
   Response: No, careful calibration measurements show that the temperature of the sample is never more than 2 K less than the recorded temperature.
4. *Question:* $SrTiO_3$ undergoes a structural transition at 105 K. Could this be responsible for the resistive transition observed at 109 K?
   Response: The authors performed a control experiment on bare, Nb-doped $SrTiO_3$ and showed that the structural transition produced a negligible signature in the R–T plot (Reference 8, their figure 3b).

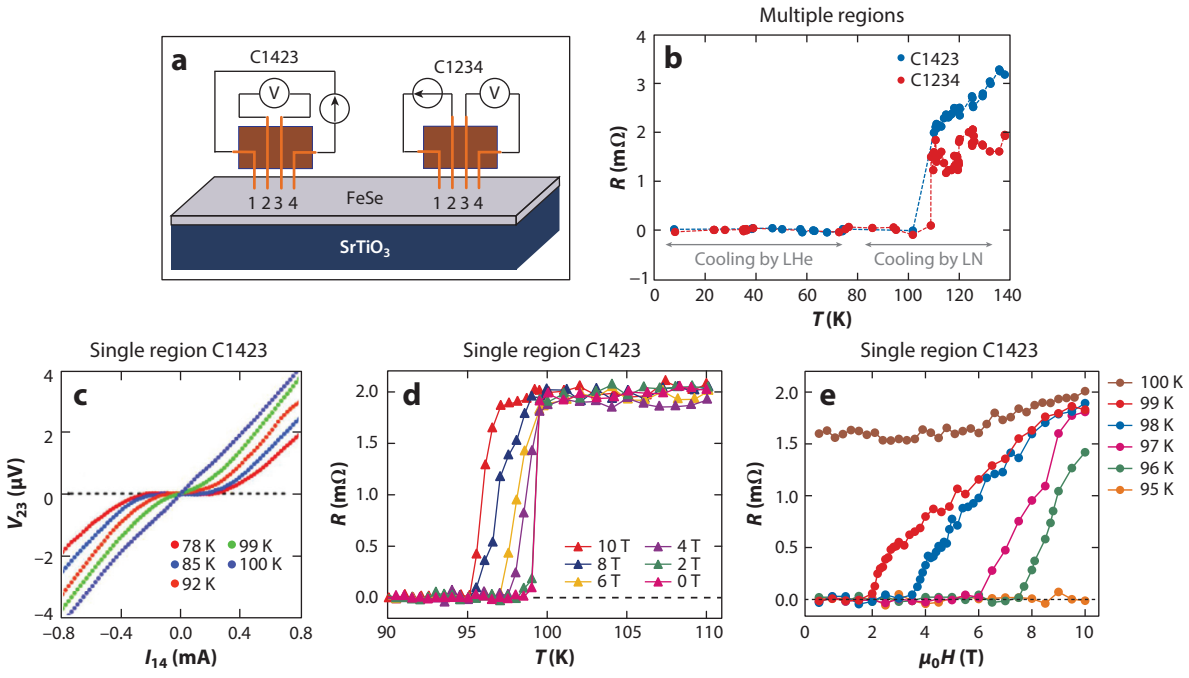

Figure 3

(*a*) Schematic of in situ, micro-four-point measurements of 1UC FeSe/$SrTiO_3$. Two possible configurations for applying a current and detecting a voltage drop are shown. Adapted from Reference 8, their figure 2, with permission. (*b*) Resistance versus temperature plot, displaying a transition temperature $T_c = 109$ K. The data points are extracted from I–V curves acquired over different regions of the sample. Adapted from Reference 8, their figure 3, with permission. (*c*) Four-point I–V curves, showing a metal-superconductor transition at a single location of the film. Adapted from Reference 8, their figure S4, with permission. (*d*) Resistance versus temperature plot, with data points extracted from I–V curves acquired at a fixed point on the sample with decreasing magnetic field and increasing temperature at each field (J.F. Ge, private communication). Adapted from Reference 8, their figure 4, with permission. (*e*) Magnetoresistance curves at various temperatures. Adapted from Reference 8, their figure 4, with permission.

5. *Question:* Don't the measured values of $T_c = 109$ K and $J_c = 1.3 \times 10^7$ A/cm^2 appear unexpectedly large?
   Response: The authors performed a control experiment on optimally doped $Bi_2Sr_2CaCu_2O_{8+\delta}$ and found $T_c = 90$ K, $J_c \sim 6{,}000$ A/cm^2, in line with expectations. Their J_c value is an order of magnitude higher than that of capped 1UC FeSe/$SrTiO_3$ films (25) but similar to that of $YBa_2Cu_3O_{7-x}$ films (32).
6. *Question:* Shouldn't there be a Berezinsky–Kosterlitz–Thouless (BKT) effect that broadens the resistive transition for a 2D superconductor? Why is the resistance drop so sharp (**Figure 3*b***), such that there are no data points within the transition (33)?
   Response: Below T_c, conduction is 2D and restricted to the superconducting FeSe monolayer. Above T_c, conduction is shorted through the Nb-doped $SrTiO_3$ substrate, which is 3D and has a much lower resistivity than normal-state FeSe. Thus, the BKT transition is masked by shorting through the metallic substrate. It is also possible that there could be a proximity effect downward into $SrTiO_3$, such that the total system is not exactly 2D. The authors were able to collect data points within this sharp transition (**Figure 3*d***).

7. *Question:* In light of the previous question, why not use an insulating $SrTiO_3$ substrate?
   Response: The authors cited practical challenges (8): "Further limits exist for detecting films grown on an insulating substrate, as the feedback required to control the contact between the film and the tip is extremely difficult."
8. *Question:* Why doesn't the resistance change when the contact separation is increased tenfold (33)?
   Response: When the probe separation distances are uniform, the resistance should scale with probe separation in both an infinite 2D conductor and a half-infinite 3D conductor. However, when the probe distances are unequal, their relationship to the overall resistance is more complicated (see Reference 8, their supplementary information).
9. *Question:* How could the resistive transition T_c be higher than the gap-closing temperature T_c measured in situ by ARPES?
   Response: ARPES averages signal over a beam spot size, but the in situ four-point probe may pick up filamentary superconductivity. Indeed, the authors found nonsuperconducting regions below T_c, but this could be attributed to intrinsic sample inhomogeneity or film damage from probes. Alternatively, if the out-of-plane coherence length is short, superconductivity might be stronger at the bottom of the FeSe triple layer than at the top. ARPES and STM measure the top, but transport accesses the lowest-resistivity part, which may be located at the buried interface.
10. *Question:* Is it possible that the apparent decreasing T_c with increasing B is simply due to gradual sample damage as B is increased?
    Response: No, the authors showed the same result with increasing B and decreasing B at a fixed location.

Despite intense scrutiny, we remain unaware of fatal flaws with the experiment by Ge et al. Nevertheless, there are increasing calls for duplication of this result, as well as complementary in situ magnetization measurements of the Meissner effect (33, 34). The latter requires specific instrumentation but will surely fill in an important piece of the puzzle.

2.2. What Are the Necessary Growth Conditions?

An accurate atomic structure is prerequisite to reliable modeling of electronic properties, and yet the former represents another significant experimental challenge for 1UC FeSe/$SrTiO_3$. Although $SrTiO_3$ is a workhorse substrate for MBE growth, it is notorious for its numerous nearly degenerate surface reconstructions that sensitively depend on preparation conditions. With the (001) surface alone, O deficiency can drive the following reconstructions: 2×1, 2×2, $c(4\times2)$, $c(4\times4)$, 4×4, $c(6\times2)$, $\sqrt{5}\times\sqrt{5}$ $R26.6°$, and $\sqrt{13}\times\sqrt{13}R33.7°$ (35). Yet some feature of this complex surface interfaced with 1UC FeSe must generate a giant enhancement in T_c. Here, we examine and clarify growth procedures for 1UC FeSe/$SrTiO_3$. The overall challenge is to identify which steps are necessary and which are supplemental. In the following section, we review various measurements of the interface atomic structure.

Figure 4 presents a flowchart with typical growth recipes for 1UC FeSe/$SrTiO_3$. The recipes can be delineated into a few primary steps, which we discuss in turn.

2.2.1. $SrTiO_3$ treatment (in situ and ex situ). Commercially available crystals of $SrTiO_3$ arrive with contaminated surfaces. In their original report, Wang et al. introduced a novel strategy to clean Nb-doped $SrTiO_3$: They annealed the substrates in their MBE chamber at 950°C for 30 minutes under a Se flux (3). This treatment produced atomically flat terraces amenable to STM imaging (albeit lacking atomic resolution). Subsequently, Bang et al. hypothesized that this process

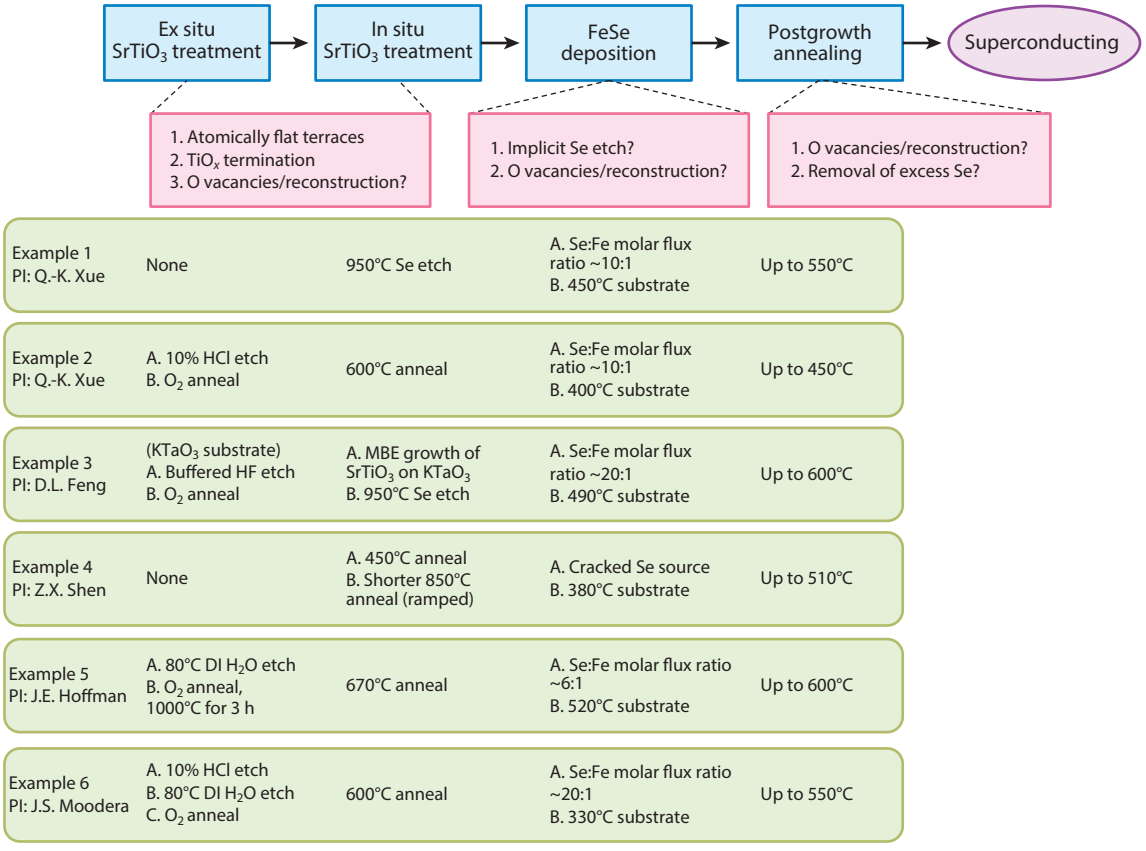

Figure 4

Flowchart of growth procedure. The blue boxes highlight primary steps that lead to superconducting 1–unit cell FeSe/$SrTiO_3$, whereas the red boxes describe the possible microscopic picture corresponding to each step. Six example recipes are given (*green boxes*): #1, Reference 3; #2, Reference 25; #3, References 5 and 24; #4, Reference 6; #5, Reference 36; and #6, Reference 31. Abbreviations: MBE, molecular beam epitaxy; PI, principal investigator.

created Se substitutions of surface O atoms (37). These Se_O substitutions would then nucleate the growth of the first FeSe monolayer, leaving behind O vacancies that stabilize binding and donate electron carriers.

Later films grown on insulating $SrTiO_3$ involved more conventional and better documented preparation protocols, involving an ex situ H_2O/acid etch followed by a high-temperature O_2 anneal in a tube furnace (25). The H_2O/acid etch is believed to preferentially remove SrO, which has ionic bonding character, and leave behind a TiO_2-terminated surface (38–40). It is thus unclear whether the previously employed Se etch is a necessary procedure for growing epitaxial FeSe on $SrTiO_3$. Despite the explicit absence of this step here, it is possible that Se_O substitutions are still generated during the deposition of 1UC FeSe.

2.2.2. FeSe deposition. To grow stoichiometric FeSe, two conditions are typically employed (12). First, because Se is significantly more volatile than Fe, the substrate temperature is set between the source temperatures: $T_{Fe} > T_{substrate} > T_{Se}$. At least for growth on inert, graphitized SiC, this condition was rationalized as follows: Impinging Fe atoms with temperature

$\sim T_{Fe}$ are adsorbed with sticking coefficient close to unity, whereas impinging Se atoms can stick only if they bind to free Fe on the substrate. Second, to compensate for high Se losses and to mitigate excess Fe clustering, typical molar flux ratios Φ_{Se}/Φ_{Fe} range from 5 to 20. We note that with these two conditions (moderate substrate temperature 400–500°C, excess Se flux), there may still be a sizeable Se chemical potential at the $SrTiO_3$ surface driving the kinds of Se reactions proposed by Bang et al., but further investigations by STM or other techniques are needed.

2.2.3. Postgrowth annealing. Post growth, the FeSe monolayer on $SrTiO_3$ becomes superconducting only after an additional vacuum anneal. He et al. used ARPES measurements to show that in this process, the FeSe monolayer is progressively doped with electron carriers (4). The electron doping induces a nonrigid band transformation that eventually leaves the FS with only electron pockets and opens up a gap. The source of electron doping remains an open question. He et al. suggested that the electron doping could arise from O vacancies in $SrTiO_3$ created during annealing. Berlijn et al. investigated the possibility of Se vacancies, but their calculations revealed Se vacancies to be hole dopants, not electron dopants (41). More recently, cross-sectional TEM imaging by Li et al. suggested the presence of interstitial Se atoms trapped at the FeSe/$SrTiO_3$ interface during growth, which are subsequently released upon annealing. The authors proposed that the removal of these interstitial Se atoms allows O vacancies in $SrTiO_3$ to effectively donate electron carriers to the FeSe monolayer (42).

Overall, some elements of correct $SrTiO_3$ pretreatment and postgrowth annealing appear necessary to produce superconducting 1UC FeSe/$SrTiO_3$, but many aspects of the growth procedure could be clarified through more systematic investigations.

2.3. What Is the Interface Structure?

We begin by comparing and contrasting three tools that have been applied to probe the interface atomic structure.

1. Scanning tunneling microscopy (STM): real-space, atomic-resolution imaging of surface
   Pro: An in situ technique commonly integrated with an MBE chamber.
   Con: An indirect technique that requires additional modeling to make inferences about the buried interface.
2. Electron diffraction [low-energy (LEED) or reflection high-energy (RHEED)]: momentum-space information of surface atomic structure
   Pro: An in situ technique that can also monitor real-time growth (RHEED).
   Con: Phase information is unavailable. The interface signal may sometimes be buried after FeSe deposition (6).
3. Transmission electron microscopy (TEM): real-space, atomic-resolution imaging of exposed cross section
   Pro: Direct atomic-resolution imaging of the interface cross section.
   Con: An ex situ technique that requires capping (commonly FeTe). As evinced in References (30, 42), Te atoms from the cap may unintentionally intermix and substitute at least the top-layer Se atoms of 1UC FeSe. The size mismatch between Se and Te can strain the monolayer film, possibly altering its original binding structure to $SrTiO_3$. Additionally, the technique averages over each column of atoms in the ~10–100-nm-thick section being studied.

2.3.1. 2×1 reconstruction. The first hint of any interface superstructure was the appearance of dark stripes with 2×1 periodicity in STM topographic images (**Figure 5*a***) (3, 37). To explain this structure, Bang et al. proposed an atomic model where half the O atoms on the surface TiO_2 layer are stripped off, and the bottom-layer Se atoms of the FeSe monolayer are laterally registered with

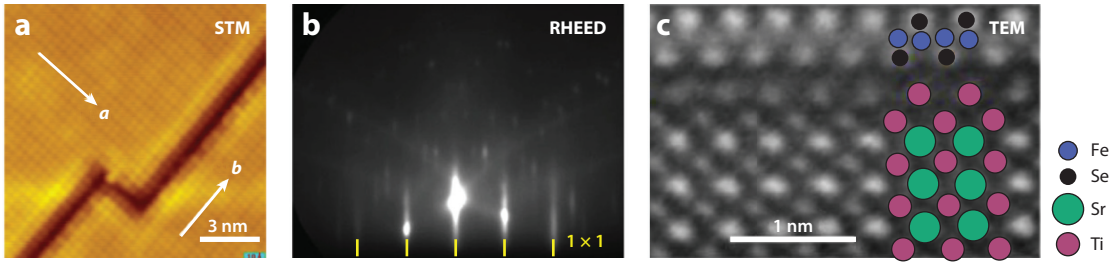

Figure 5

Measurements of interface structure. (*a*) Scanning tunneling microscopy (STM) topographic image showing orthogonal domains with dark stripes of 2×1 periodicity. Across the trench, there is a half–unit cell (UC) phase shift. Adapted from Reference 37, their figure 1, with permission. (*b*) Reflection high-energy electron diffraction (RHEED) diffraction patterns of treated $SrTiO_3$ prior to FeSe deposition, exhibiting reconstruction spots. Adapted from Reference 6, their extended data figure 1, with permission. (*c*) Cross-sectional transmission electron microscopy (TEM) image of FeTe/1UC FeSe/$SrTiO_3$, revealing that the $SrTiO_3$ is terminated with a double-TiO_x layer (atomic model is overlaid). Adapted from Reference 42, their figure 2, with permission.

the O vacancy sites (37). The authors argued that such an arrangement could increase the binding energy, electron-dope the FeSe monolayer, and cause the FeSe monolayer to relax with a 2×1 superstructure. In addition, because there are two equivalent O sites within a TiO_2 UC, the model could naturally explain the observation of half-UC phase shifts that occur either discontinuously at a trench (43) (**Figure 5*a***) or continuously within a few nanometers of a domain boundary (44).

As a word of caution, the 2×1 stripes have not been universally observed. They are absent in atomic force microscopy topographies (45), which might point to an electronic origin of the stripes, and are also absent in STM topographies of samples prepared in different ways (23, 36).

2.3.2. More reconstructions. Lee et al. grew 1UC FeSe on $SrTiO_3$ with neither in situ Se etching nor ex situ treatment (6). They simply annealed as-bought substrates up to 830°C in their MBE chamber, until RHEED measurements detected superstructure spots, typically but not necessarily $\sqrt{5}\times\sqrt{5}$ (46) (**Figure 5*b***). Subsequent deposition of FeSe and postgrowth annealing resulted in superconducting samples with 1×1 diffraction spots.

Peng et al. found a qualitatively different behavior in 1UC FeSe/$BaTiO_3$ (22). After annealing $BaTiO_3$ at 950°C under Se flux, their LEED images exhibited 3×3 spots. Curiously, growth of 1UC FeSe produced three distinct domains: one domain commensurate with the $BaTiO_3$ 1×1 UC, with expanded lattice constant 3.99 Å, and two domains rotated by ±18.5°, commensurate with a $BaTiO_3$ 3×3 supercell, with smaller lattice constant 3.78 Å. Furthermore, ARPES detected superconducting gaps in all three regions, with closing temperature T_c in the range of 70–75 K.

More recent experiments have detected superconducting gaps in 1UC FeSe on $SrTiO_3$ (110) (47, 48), anatase TiO_2 (001) (49), and rutile TiO_2 (50), with different lattice constants and surface reconstructions (prior to growth). Taken together (**Table 2**), the variety may imply that neither lattice constant nor the lateral atomic registry between 1UC FeSe and its underlying substrate are critical factors behind the enhanced superconductivity of this heterostructure.

2.3.3. Double-TiO_x termination. Perhaps what matters is the vertical structure of the interface. Using cross-sectional TEM, Li et al. (42) imaged a double-TiO_x termination at the interface of FeTe/1UC FeSe/$SrTiO_3$ (**Figure 5*c***). Zou et al. (51) also uncovered a double-TiO_x termination using X-ray diffraction, LEED, and RHEED. Although such termination had long been proposed as a candidate model for the 2×1 surface reconstruction (52), it had largely been neglected in atomic models of 1UC FeSe/$SrTiO_3$ until this point. Roughly speaking, the extra TiO_x termination is half

Table 2 Reconstructions observed in various superconducting FeSe/(A)TiO_x heterostructures

Substrate	Lattice constant (bulk FeSe: $a_0 = 3.77$ Å)	Reconstruction (method)	Reference
$SrTiO_3$ (001)	$a_0 = 3.90$ Å	2×1 (STM) $\sqrt{5}\times\sqrt{5}$ (RHEED) $\sqrt{13}\times\sqrt{13}$ (various)	3, 37, 43–45 6, 46 51
$SrTiO_3$ (110)	$a_0 = 3.90$ Å $b_0 = 5.52$ Å	4×1 (STM) 6×1 (STM) 3×1 (LEED)	47 47 48
$BaTiO_3$ (001)	$a_0 = 3.99$ Å	3×3 (LEED)	24
Anatase TiO_2 (001)	$a_0 = 3.78$ Å	4×1 (STM)	49

Abbreviations: LEED, low-energy electron diffraction; RHEED, reflection high-energy electron diffraction; STM, scanning tunneling microscopy.

as polar as a bulk TiO_2 layer and helps $SrTiO_3$ mitigate a divergence of the electrostatic potential toward its bulk (53). Structural and ferroelectric properties are likely modified near this double-TiO_x termination. Zou et al. argued that the double-TiO_x termination facilitates epitaxial growth of FeSe through stronger binding and also improves charge transfer from oxygen vacancies (51).

Li et al. also used TEM imaging to extract the structural parameters of their FeTe-capped sample. They found the 1UC FeSe to have a 9.5% reduced chalcogen height with 2.5% in-plane lattice tensile strain (compared with bulk values). Furthermore, within a ~10-nm cross section, the authors imaged a lateral half-UC shift between the bottom Se atoms and topmost Ti atoms. If this feature is characteristic of uncapped 1UC FeSe/$SrTiO_3$, then it suggests that the heterostructure has local bond disorder due to incommensurate lattices. We note that STM dI/dV measurements do reveal spectral and gap inhomogeneity even in pristine regions of FeSe with no in-plane, atomic-scale defects (54). Further systematic investigations and correlation of disorder with growth procedures is needed.

3. ELECTRONIC STRUCTURE AND PAIRING

Having surveyed a range of experiments characterizing the basic properties of 1UC FeSe/$SrTiO_3$, we turn to the question of electronic structure and pairing. Superconductors are typically categorized into one of two paradigms: conventional or unconventional (**Table 3**). In a conventional superconductor, electrons are bound into Cooper pairs by attractive interactions mediated by phonons. The resulting energy gap has s-wave angular symmetry and a uniform sign throughout the BZ. In an unconventional superconductor, many believe that quantum fluctuations from a proximate phase (e.g., magnetism) provide the glue to bind electrons. Because these fluctuations are often repulsive, the resulting gap function harbors sign changes throughout the BZ (to be further discussed in Section 3.4). This latter class of superconductors, which includes the cuprates

Table 3 Two paradigms of superconductivity

	Conventional	Unconventional
Maximum T_c	203 K Pressurized H_3S (55)	164 K Pressurized $HgBa_2Ca_2Cu_3O_{8+\delta}$ (56)
Pairing mechanism	Phononic	Electronic (magnetic/orbital)
Gap structure	Sign-preserving	Sign-changing

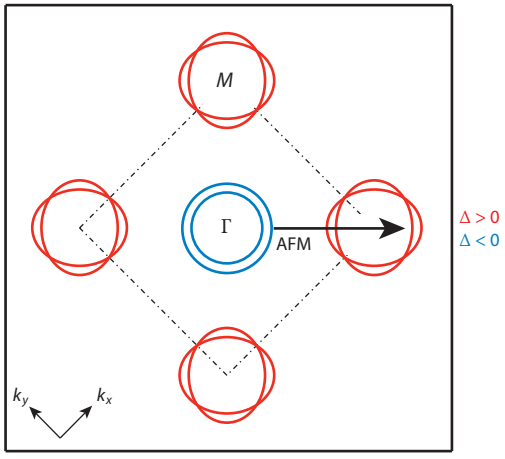

Figure 6

Schematic of unconventional s_{+-} pairing proposed for iron pnictide superconductors (57, 58). The generic Fermi surface of these compounds consists of electron pockets at the Brillouin zone (BZ) corner M and hole pockets at the zone center Γ. The dashed line encloses the 2-Fe BZ. The electron and hole pockets are nested by an antiferromagnetic (AFM) wave vector, which can result in pairing if the gap function has one sign on the electron pockets (*red*, $\Delta > 0$) and the opposite sign on the hole pockets (*blue*, $\Delta < 0$).

and iron pnictides, has long been associated with higher T_c values. However, the tables have turned with the recent discovery of 203-K conventional superconductivity in pressurized H_3S (55).

Within months of the 2008 discovery of iron pnictide superconductors, Mazin et al. (57) and Kuroki et al. (58) proposed an unconventional mechanism of pairing in these compounds. The basic premise was that first, the electron–phonon coupling constant was too small (57, 59); second, the proximity of the superconductor to an antiferromagnetic metal hinted at the role of spin fluctuations; and third, the multiband FS of these compounds, comprising electron pockets at the zone corner M and hole pockets at the zone center Γ, could be crucial. The authors then argued that repulsive spin fluctuations, with wave vector spanning the separated electron and hole pockets, could pair electrons if the gap function reversed sign across the pockets with an overall "s_{+-}" symmetry (**Figure 6**). Though not free from controversy (60), this framework prevailed in the early years of iron pnictide superconductors.

Fast-forwarding to the present, 1UC FeSe/$SrTiO_3$ poses several theoretical conundrums. First, its FS includes M electron pockets (**Figure 2*e***) but not the Γ hole pockets necessary for s_{+-} pairing. Second, it appears to exhibit traits of both conventionality and unconventionality. In this section, we review contrasting indications for both phononic (Section 3.1) and electronic (spin/orbital, Section 3.2) mechanisms of pairing. We then evaluate ARPES and STM measurements of gap symmetry and structure (Subsection 3.3). Finally, we discuss multiband, multiboson scenarios of pairing that enable phonons and spin/orbital fluctuations to operate constructively to enhance T_c (Section 3.4). These latter ideas are far from being a fait accompli but exemplify a potential "best-of-both-worlds" path toward creating higher-T_c superconductors.

3.1. Phononic Mechanisms

In their original report, the discoverers of 1UC FeSe/$SrTiO_3$ proposed some sort of interface-enhanced electron–phonon coupling as the mechanism for high-T_c superconductivity. Here, we discuss subsequent ARPES experiments by Lee et al. that lent support to this notion (6).

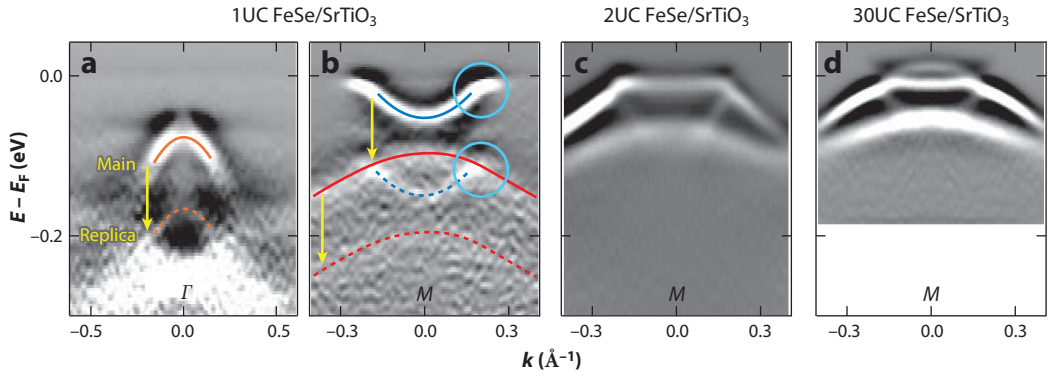

Figure 7

(*a*,*b*) Angle-resolved photoemission spectroscopy (ARPES) high-symmetry cuts of 1UC FeSe/$SrTiO_3$ showing primary electronic bands (*solid line overlays*) and corresponding "replica" bands (*dashed line overlays*)—fainter duplicates of the primary bands, shifted down by 100 meV (*yellow arrows*). These replica features suggest a $\mathbf{q} \sim 0$ coupling to $SrTiO_3$ phonon mode. The blue circles highlight the duplication of a back-bending dispersion in the primary band as a superconducting gap opens near the Fermi energy. (*c*,*d*) ARPES high-symmetry cuts of 2UC and 30UC FeSe/$SrTiO_3$, showing the absence of replica bands. Adapted from Reference 6, their figure 3, with permission.

3.1.1. Replica bands. In their ARPES measurements, Lee et al. discovered that each primary electronic band of 1UC FeSe/$SrTiO_3$ possessed a fainter replica band offset by 100 meV (6). These faint bands were near-duplicates of their primary counterparts, without being offset in momentum or smeared (**Figure 7*a*,*b***). In addition, the replica bands persisted at least to 120 K, well above the gap-opening temperature ($T_c = 58 \pm 7$ K). Such replicas were absent in FeSe films of two UCs or thicker (**Figure 7*c*,*d***), pointing to an interfacial origin of these features. Similar phenomenology was observed by Peng et al. in 1UC FeSe/$BaTiO_3$ (22).

In their interpretation of the replica bands, Lee et al. first excluded the possibility of quantum-well states arising from 2D confinement. There is no reason for such states to have identical dispersions. Furthermore, quantum-well states exhibit a well-behaved dependence on layer, in contrast to the abrupt disappearance of replica bands in 2UC FeSe/$SrTiO_3$. Instead, the authors attributed the replica bands to bosonic shake-off, in analogy to vibrational shake-off observed in photoemission spectroscopy of H_2 molecules. They identified the boson with an optical O phonon band calculated for bulk $SrTiO_3$ (61). Subsequent calculations of slab $SrTiO_3$ pointed to a surface phonon mode involving polar vibrations of vertical Ti–O bonds (62). These theoretical comparisons were later corroborated by ARPES measurements that also found replica bands on bare $SrTiO_3$ (63). However, for an electron–phonon coupling $g(\mathbf{q})$ to produce nearly identical bands with no momentum smearing, it must be sharply peaked at $\mathbf{q} = 0$. This differs from the usual assumption of a constant $g(\mathbf{q})$ in theories of phonon-mediated superconductivity, and some modeling is needed to understand its origin.

3.1.2. Model of interface electron–phonon coupling. To explain how the electron–phonon coupling $g(\mathbf{q})$ could become sharply peaked at $\mathbf{q} = 0$, Lee et al. presented the following model (6, 64): Assume we have a 2D sheet of FeSe at $z = 0$ and a layer of dipole moments below at the $SrTiO_3$ surface, $z = -h_0$ (**Figure 8**). The dipole moments come from vertical stretching of surface Ti–O bonds and are represented by $\delta p_z(x, y, -h_0)$. From an electrostatics calculation,

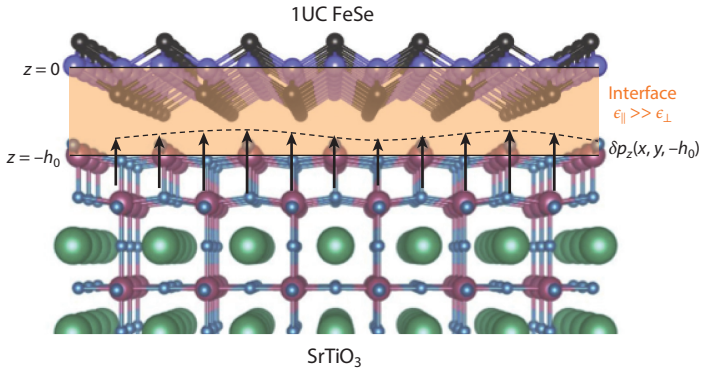

Figure 8

Electrostatic model of interface electron–phonon coupling (6, 64), consisting of a 2D layer of FeSe at $z=0$ and a layer of vertical dipole moments $\delta p_z(x, y, -h_0)$ at the $SrTiO_3$ surface, $z=-h_0$. If the interface region has anisotropic dielectric constants, $\epsilon_\parallel \gg \epsilon_\perp$, then the induced potential $\delta\Phi$ is exponentially peaked at $\mathbf{q}=0$.

these moments induce a potential at the FeSe layer,

$$\delta\Phi(x,y,0) = \frac{\epsilon_\parallel h_0}{\epsilon_\perp^{3/2}} \int \mathrm{d}x'\mathrm{d}y' \frac{\delta p_z(x',y',-h_0)}{[\epsilon_\parallel h_0^2/\epsilon_\perp + (x-x')^2 + (y-y')^2]^{3/2}}, \quad (1)$$

where $\epsilon_\parallel$, $\epsilon_\perp$ are the in-plane and perpendicular dielectric constants in the interface region, respectively. Taking the Fourier transform yields

$$\delta\Phi(\mathbf{q},0) = \sqrt{\frac{\epsilon_\parallel}{\epsilon_\perp}} \frac{2\pi}{\sqrt{\epsilon_\perp}} \exp\left(-|\mathbf{q}|h_0\sqrt{\epsilon_\parallel/\epsilon_\perp}\right)\delta p_z(\mathbf{q},-h_0). \quad (2)$$

It follows that $g(\mathbf{q}) \propto \delta\Phi(\mathbf{q},0) \propto \exp(-|\mathbf{q}|/q_0)$, where $q_0^{-1} = h_0\sqrt{\epsilon_\parallel/\epsilon_\perp}$. Intuitively, the $\mathbf{q}\sim 0$ coupling hinges upon (*a*) the FeSe monolayer being sufficiently removed from the dipole layer (large h_0) and (*b*) the interface region screening lateral charge imbalance much more effectively than vertical charge imbalance (large $\epsilon_\parallel/\epsilon_\perp$).

Calculations by Rademaker et al. showed that a ratio of $q_0/k_F \sim 0.1$ was needed for replica bands to duplicate primary band features without significant momentum smearing (65). If we take k_F to be 0.20 $Å^{-1}$ (17) and h_0 to be 4.9 Å (42), the distance between the surface TiO_2 layer and the Fe plane, then $1/(h_0k_F) \sim 1$, and we require $\epsilon_\parallel/\epsilon_\perp \sim 100$ in the interface region. Although one should be wary of interpreting the model interface too literally, an argument suggests that it should contain contributions from both $SrTiO_3$ and FeSe, with the former having $\epsilon_\parallel^{SrTiO_3} \sim \epsilon_\perp^{SrTiO_3}$ in its 3D bulk limit and the latter having $\epsilon_\parallel^{FeSe} \gg \epsilon_\perp^{FeSe}$ due to its 2D nature (64).

Alternative speculations regarding the replica bands include O impurity bands (66) or some form of Raman scattering involving $SrTiO_3$ phonon modes (S.A. Kivelson, private communication). No model details have been presented for impurity bands, and it is unclear whether sufficient cross section and viable selection rules exist for Raman scattering. Peaks and dips have been detected in STM filled- and empty-state $\mathrm{d}^2I/\mathrm{d}V^2$ spectra (see the supplemental material of Reference 36), but the authors have not confirmed their identity as replica bands.

3.1.3. FeSe phonon modes. In their initial STM measurements of 1UC FeSe/$SrTiO_3$, Wang et al. reported two gaps in the $\mathrm{d}I/\mathrm{d}V$ point spectrum, at 9 meV and 20.1 meV, respectively

(3). This finding appeared to contradict early ARPES measurements of a single isotropic gap on the zone corner electron pockets, with $\Delta = 13 \pm 2$ meV in one film and 15 ± 2 meV in another film (17). Coh et al. offered an alternative explanation for the double-gap signature in terms of two FeSe phonon modes, which they argued could enhance T_c when a monolayer of FeSe is locked to a $SrTiO_3$ substrate (67). Following this report, Tang et al. examined d^2I/dV^2 point spectra of 1UC FeSe/$SrTiO_3$ and K-coated 2–4UC FeSe/$SrTiO_3$ (68). They identified positive-energy dips around 11 meV and 21 meV as FeSe phonon modes.

3.2. Electronic Mechanisms

A feature of the interface phonon-coupling model is that it does not depend at all on 1UC FeSe, as long as the heterostructure has an interface dielectric constant that is sufficiently anisotropic. On one hand, such generality could be desirable for reproducing this mechanism in other systems. On the other hand, the model leaves open the possibility of preexisting pairing interactions within FeSe that are subsequently strengthened by $SrTiO_3$.

Two foil systems suggest that interface phonon coupling plays a secondary role to a primary pairing mechanism within FeSe that is enhanced by electron doping. The first is an FeSe-intercalate, $(Li_{1-x}Fe_x)OHFeSe$. Fe_{Li} antisite substitutions increase electron transfer from buffer LiOH layers to FeSe (69), resulting in 40-K superconductivity (70). Importantly, ARPES and STM measurements resolved low-energy bands that are nearly identical to those of 1UC FeSe/$SrTiO_3$ and gaps of similar magnitudes (71–74); however, no replica bands were visible. The second system involves coating FeSe with K adatoms, which inject electrons into the surface FeSe layer (68, 75–80). The resulting superconducting phase has a gap-closing temperature up to 48 K, close to the 65-K value of 1UC FeSe/$SrTiO_3$. The electronic transition induced by progressive K deposition is rather rich and provides clues of unconventional mechanisms of pairing.

3.2.1. Clues from the electron-doping phase diagram. In the paradigm of unconventional superconductors, pairing is likely mediated by quantum fluctuations from nearby electronic phases. Hence, we glean inspiration from the electron-doping phase diagram of FeSe, keeping in mind that it may not be fully representative of 1UC FeSe/$SrTiO_3$.

The first striking feature in the electron-doping phase diagram of FeSe is that T_c evolves through two domes (80): a low-T_c phase is first suppressed, eventually giving way to a higher-T_c phase (**Figure 9**). In general, domes are hallmarks of unconventional superconductivity, less naturally explained within a purely phononic framework (66). Song et al. also found that the higher-T_c phase is insensitive to the disorder of nonmagnetic K adatoms, a point whose implications we revisit in Section 3.3.

A second observation is that nematic order is suppressed preceding the high-T_c phase (75, 76), although a smaller overlapping tail of the nematic phase may persist due to remnant uniaxial strain from underlying bulk FeSe (77). Nematic order is generally defined as broken rotational symmetry that preserves the translational symmetry of the crystal. In stoichiometric FeSe, nematic order is manifested as a small orthorhombic distortion (85) and a large splitting of the Fe $3d_{xz}$ and $3d_{yz}$ bands (5, 18–21, 86) without concomitant magnetic order (87). Given the proximity and possible overlap of the nematic phase, it is tempting to ask whether nematic quantum criticality could be at play. Nematic fluctuations would provide attractive $\mathbf{q} \sim 0$ interactions that help bind electrons (88–93), much like the aforementioned $SrTiO_3$ phonons.

3.2.2. Nematic fluctuations. Because 1UC FeSe bound to $SrTiO_3$ is nominally tetragonal, nematic order should be globally suppressed. However, if there truly exists a large underlying

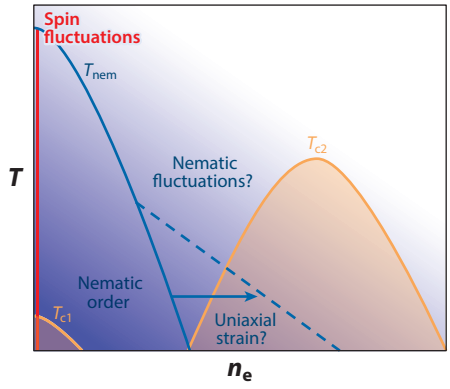

Figure 9

Schematic phase diagram of electron-doped FeSe, consisting of two domes of superconductivity and the possibility of nematic fluctuations. Adapted from References 75, 77, 80, and 81 with permission. The existence of spin fluctuations in stoichiometric FeSe was reported in References 82–84.

nematic susceptibility that produces fluctuations, then nanoscale patches of such fluctuations might be pinned around crystalline imperfections that locally break tetragonal symmetry.

Using STM as a nanoscale probe, Huang et al. investigated quasiparticle interference (QPI) patterns generated around anisotropic defects in 1UC FeSe/$SrTiO_3$ (54) (**Figure 10**). Because QPI anisotropy can arise from random disorder or experimental artifacts, the authors developed a realistic, T-matrix model to specifically detect orbital anisotropy of Fe $3d_{xz}$ and $3d_{yz}$ bands. By sampling multiple spatial regions of a film, they excluded xz/yz orbital ordering with domain size larger than $\delta r^2 = 20$ nm $\times$ 20 nm, xz/yz Fermi wave vector difference larger than $\delta k = 0.014\,\pi$, and energy splitting larger than $\delta E = 3.5$ meV. The lack of detectable ordering pinned around defects disfavors scenarios of a proximate nematic quantum critical point in 1UC FeSe/$SrTiO_3$, in contrast to K-coated FeSe (**Figure 9**).

3.2.3. Spin fluctuations. Given the importance of spin fluctuations in many iron pnictide superconductors, their role in pairing should also be considered in 1UC FeSe/$SrTiO_3$ (94). Several inelastic neutron scattering measurements found that in stoichiometric FeSe, there are stripe spin fluctuations that are enhanced below the orthorhombic transition temperature (82–84) (**Figure 9**). However, magnetic order is absent, owing to some sort of frustration (95–97) or quadrupolar order (98). The nature of spin excitations in 1UC FeSe/$SrTiO_3$ remains an important open question, especially because both doping and the Se height may tune exchange interactions. Some experimental ingenuity is required, as ex situ neutron scattering measurements are likely not feasible on 1UC films. One possible approach is the use of STM to map the magnetic-field dependence of impurity signatures in comparison with theoretical modeling (99).

3.3. Gap Symmetry and Structure

We shift gears and consider pairing from the viewpoint of gap symmetry and structure. In general, such questions have proven more challenging to address in the iron-based superconductors than in the cuprates. Unlike the cuprates, with a single Cu d band and universal $d_{x^2-y^2}$ gap symmetry, the multiband FS the of iron-based superconductors can allow a variety of gap structures across their member compounds. Even within the same compound, such as KFe_2As_2, different pairing symmetries can be tuned by pressure (100). To add to the challenge, many candidate gap structures

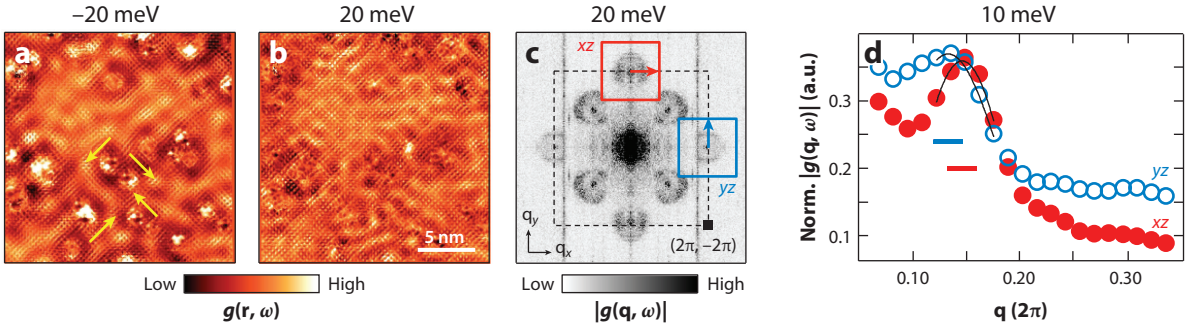

Figure 10

Bounds on nanoscale nematicity in 1UC FeSe/$SrTiO_3$. (*a*,*b*) Scanning tunneling microscopy conductance maps $g(\mathbf{r}, \omega)$ over a region of 1UC FeSe/$SrTiO_3$ containing several atomic-scale defects, revealing dispersive quasiparticle interference (QPI) patterns. The prevalent defects are anisotropic and appear in four possible orientations (*yellow arrows*). Panel *a* adapted from Reference 54, their figure 12, and panel *b* adapted from Reference 54, their figure 1, with permission. (*c*) Fourier transform amplitude $|g(\mathbf{q}, \omega)|$ of panel *b*. The red and blue boxes enclose ring intensities that arise from scattering between Fermi electron pocket states of Fe $3d_{xz}$ and $3d_{yz}$ orbital characters, respectively. Adapted from Reference 54, their figure 2, with permission. (*d*) Normalized line cuts across the arrows as shown in panel *c*, used to compare *xz*/*yz* scattering wave vectors. The horizontal bars mark the peak locations determined from Gaussian fits (*solid lines*) with inherent resolution $\delta q = 0.028\ \pi$. No signature of orbital nematicity was detected. Adapted from Reference 54, their figure 5,with permission.

share the same angular symmetry (101) and thus cannot be differentiated by the corner junction experiments that proved instrumental in revealing the *d*-wave gap of $YBa_2Cu_3O_{7-x}$ (102). ARPES can resolve gap magnitudes on each specific band but not their signs. STM QPI measurements carry phase-sensitive information but can be challenging to interpret or normalize (103).

With these complications in mind, there is less likely to be a clear,"smoking-gun" experiment revealing the gap symmetry of 1UC FeSe/$SrTiO_3$. A more likely scenario is that through multiple experimental measurements, consensus will begin to converge upon a candidate gap function.

3.3.1. The candidates. Given the FS of 1UC FeSe/$SrTiO_3$, with only electron pockets, the primary gap symmetry candidates are "plain" *s*, "nodeless" *d*, "bonding–antibonding" *s*, and "incipient" s_{+-} (**Figure 11**). Nodal candidates are inconsistent with the fully gapped structures detected by STM and ARPES (**Figure 2*b***).

Plain *s* gap symmetry (**Figure 11*a*,*b***) is discussed in Subsection 3.3.3. Nodeless *d* (**Figure 11*c*,*d***), which appears most similar to the gap in cuprates, is strictly defined in a 1-Fe, "pseudocrystal momentum" BZ ($\tilde{\mathbf{k}}$) that only exists when FeSe has exact glide-plane symmetry. When the gap structure is folded into the proper 2-Fe BZ, it is no longer *d*-wave with respect to regular crystal momentum ($\mathbf{k}$). In addition, nodes are technically created when opposite-sign gaps meet at the pocket crossings (104). However, based on microscopic details, the nodal quasiparticle weight could be weak and elude spectroscopic detection (105, 106).

If the folded pockets in the 2-Fe BZ hybridize and detach from each other, then nodes will certainly be avoided, leading to a bonding–antibonding *s* scenario (**Figure 11*e***). Here, the inner and outer pockets host gaps of opposite sign.

Incipient s_{+-} posits that an opposite-sign gap develops on a sunken zone center hole pocket (**Figure 11*f*,*g***). In the weak-coupling limit, such a gap can still be sizeable (107), the reasons for which we discuss in Subsection 3.4.

3.3.2. Angle-resolved photoemission spectroscopy measurements. Early ARPES investigations of 1UC FeSe/$SrTiO_3$ reported isotropic gaps ($\Delta = 13$–15 meV) on nearly circular electron

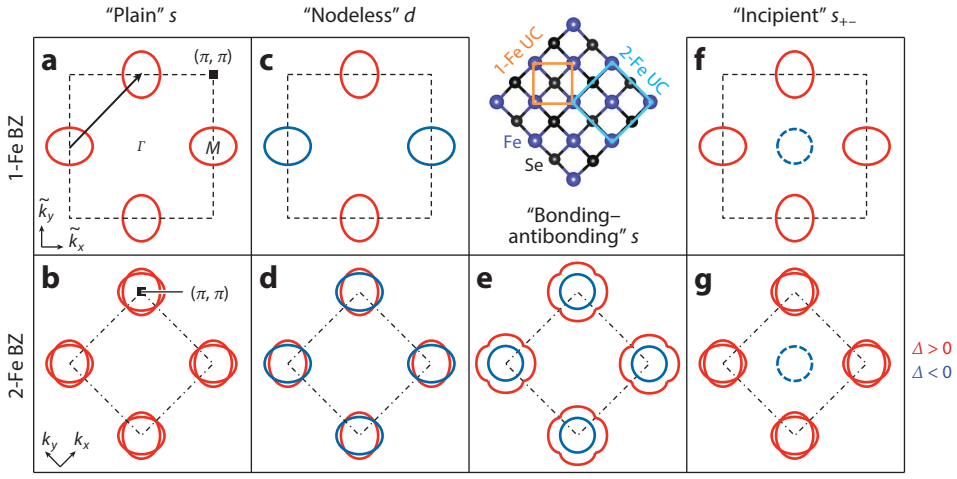

Figure 11

Gap symmetry candidates for 1UC FeSe/$SrTiO_3$. The top row depicts these structures in a 1-Fe Brillouin zone (BZ) ($\tilde{\mathbf{k}}$), and the bottom row depicts their folded counterparts in the 2-Fe BZ ($\mathbf{k}$). The arrow in panel *a* marks the folding wave vector, and the schematic illustrates the 1-Fe and 2-Fe unit cells (UCs). Note that the "bonding–antibonding" *s* structure in panel *e* cannot be unfolded. The dashed pockets for "incipient" s_{+-} in panels *f* and *g* represent bands that lie completely below (or above) the Fermi energy.

pockets (4–6, 17). To resolve finer structure, Peng et al. grew 1UC FeSe on $SrTiO_3/KTaO_3$, whose expanded lattice constant increased pocket ellipticity (24). Alternatively, Zhang et al. changed photon polarizations to selectively probe bands of different orbital characters (108). In both cases, the authors observed two pockets at each corner (main and folded), with no signs of hybridization (**Figure 12*a–c***). Momentum distribution cuts across the intersection of the main and folded pockets revealed a single band, with no detectable splitting. Furthermore, gap measurements on equivalent segments of the main and folded pockets showed identical structure. Such lack of sizeable hybridization remains to be understood, given that both spin–orbit coupling or the $SrTiO_3$ substrate can break glide-plane symmetry. More importantly, it also disfavors scenarios of bonding–antibonding *s*-wave pairing. The authors in both reports also resolved gap anisotropy, with minima directed along the Fe–Se axes. These measurements will provide useful feedback for theoretical gap function calculations.

3.3.3. Scanning tunneling microscopy measurements. Fan et al. employed a multipronged STM approach, involving phase-sensitive QPI and defect imaging, to build support for plain *s*-wave superconductivity in 1UC FeSe/$SrTiO_3$ (44). In particular, the authors found that magnetic adatoms (Cr, Mn) induced in-gap bound states, whereas nonmagnetic adatoms did not (Zn, Ag, K) (**Figure 12*d–g***). This observation is consistent with an underlying gap structure without sign changes but not a fool-proof guarantee of such. Anderson's theorem states that a superconductor with a sign-preserving gap should be robust against the disorder of nonmagnetic impurities. Taken in its equivalent, contrapositive form, the observation of in-gap states induced by nonmagnetic impurities would thereby signal a sign-changing gap. However, the converse statement (robustness against nonmagnetic impurities $\Longrightarrow$ sign-preserving gap) is not logically identical to the original theorem, so it lacks a"smoking-gun" nature (101, 109). In the case of 1UC FeSe/$SrTiO_3$, with the nodeless *d* and bonding–antibonding *s* gap structures, the opposite-sign gaps reside on normal-state Fermi pockets with different orbital characters. Given that the impurities in the Fan et al.

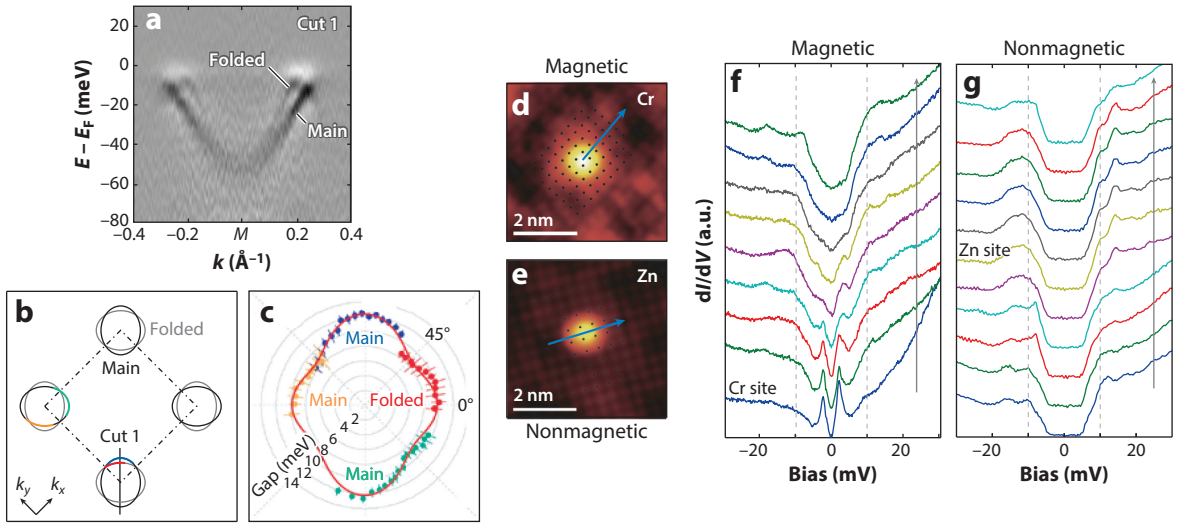

Figure 12

(*a–c*) Angle-resolved photoemission spectroscopy measurements of gap anisotropy. The nearly identical gap structures on equivalent segments of the main and folded pockets (*red* and *orange cuts*) disfavor scenarios of "bonding–antibonding" *s*-wave pairing. Panel *a* adapted from Reference 108, their figure 2, and panel *c* adapted from Reference 108, their figure 4, with permission. (*d–g*) Scanning tunneling microscopy dI/dV line cuts across magnetic (Cr) and nonmagnetic (Zn) adatoms. In-gap states are produced in the former, whereas no changes are visible in the latter. These observations favor "plain" *s*-wave symmetry. Adapted from Reference 44 with permission.

experiment lie outside the Fe plane, they may have had insufficient interorbital scattering strength to produce a pair-breaking effect. This complication is alleviated in the case of s_{+-} pairing in the iron pnictides. Because both the electron and hole pockets hosting opposite-sign gaps share the same orbital characters, interband scattering mixing the signs is easier. Despite these caveats, the preponderance of current experiments favor same-sign gaps on all Fermi pockets of 1UC FeSe/$SrTiO_3$ above the other possibilities.

3.4. Multiband, Multiboson Scenarios of Pairing

In this final section, we examine pairing scenarios in which multiple bosons work cooperatively across multiple bands to boost T_c. More specifically, we consider various ways in which attractive interactions (e.g., mediated by phonons) and repulsive interactions (e.g., mediated by spin fluctuations) can fit under the same roof in 1UC FeSe/$SrTiO_3$ (6, 92, 107, 110).

The basic picture can be explained from the $T = 0$ gap equation of a one-band superconductor in the weak-coupling limit:

$$\Delta_{\mathbf{k}} = -\sum_{\mathbf{k}'} \frac{V_{\mathbf{k},\mathbf{k}'}\Delta_{\mathbf{k}'}}{2E_{\mathbf{k}'}}. \tag{3}$$

Here, $V_{\mathbf{k},\mathbf{k}'}$ is an effective potential that scatters a Cooper pair from $(\mathbf{k}\uparrow, -\mathbf{k}\downarrow)$ to $(\mathbf{k}'\uparrow, -\mathbf{k}'\downarrow)$, $E_{\mathbf{k}'} = \sqrt{\xi_{\mathbf{k}'}^2 + |\Delta_{\mathbf{k}'}^2|} > 0$ is the Bogoliubov quasiparticle energy, $\xi_{\mathbf{k}'}$ is the normal-state quasiparticle energy, and $\Delta_{\mathbf{k}}$ is the gap function. Because any such $\Delta_{\mathbf{k}}$ must obey Equation 3 self-consistently, its form is determined by $V_{\mathbf{k},\mathbf{k}'}$ as follows:

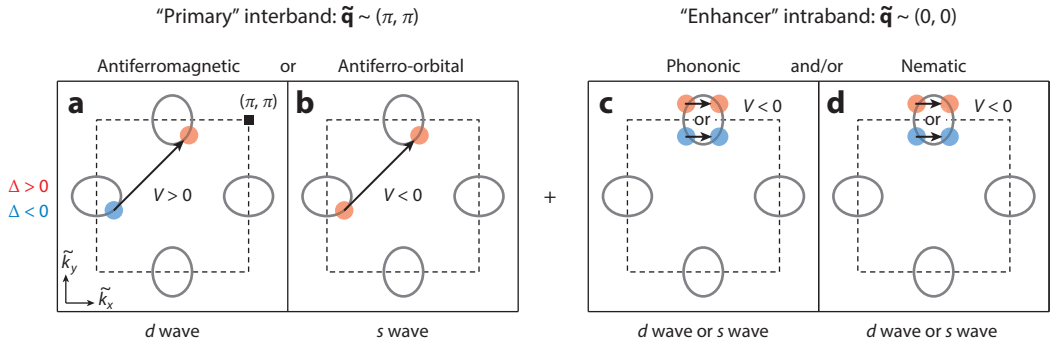

Figure 13

Multiband, multiboson scenarios of pairing in 1UC FeSe/$SrTiO_3$. For simplicity, we work in a 1-Fe, pseudocrystal momentum ($\tilde{\mathbf{k}}$) Brillouin zone. (*a*,*b*) Step 1: The gap (Δ) symmetry is determined by a "primary" interband interaction, peaked around $\tilde{\mathbf{q}} = (\pi, \pi)$, which may be attractive ($V < 0$) or repulsive ($V > 0$). (*c*,*d*) Step 2: T_c is further boosted by "enhancer" intraband interactions that are attractive. Due to their forward-scattering nature [i.e., peaked around $\tilde{\mathbf{q}} = (0, 0)$], they can raise T_c for any gap symmetry.

1. Attractive interactions ($V_{\mathbf{k},\mathbf{k}'} < 0$) increase the gap amplitude if they connect segments of the FS hosting same-sign gaps ($\Delta_{\mathbf{k}} > 0$ and $\Delta_{\mathbf{k}'} > 0$, or $\Delta_{\mathbf{k}} < 0$ and $\Delta_{\mathbf{k}'} < 0$).
2. Repulsive interactions ($V_{\mathbf{k},\mathbf{k}'} > 0$) increase the gap amplitude if they connect segments of the FS hosting opposite-sign gaps ($\Delta_{\mathbf{k}} > 0$ and $\Delta_{\mathbf{k}'} < 0$, or $\Delta_{\mathbf{k}} < 0$ and $\Delta_{\mathbf{k}'} > 0$).

Attractive and repulsive interactions can therefore simultaneously increase the gap amplitude, if the interactions connect different segments of the FS with appropriate signs in the gap function. In the limit of forward scattering ($\mathbf{k} = \mathbf{k}'$), attractive interactions have the form $V_{\mathbf{k},\mathbf{k}'} \propto -\delta_{\mathbf{k},\mathbf{k}'}$, and from Equation 3, increase the gap amplitude irrespective of the gap sign or functional form.

Figure 13 illustrates a pairing framework for 1UC FeSe/$SrTiO_3$ involving multiple bosons. We postulate the existence of a primary interband interaction peaked around $\tilde{\mathbf{q}} = (\pi, \pi)$, connecting the disparate electron pockets and dictating the overall gap symmetry (**Figure 13*a*,*b***). This interaction could be a repulsive antiferromagnetic spin fluctuation, a stabilizing *d*-wave pairing, or an attractive antiferro-orbital fluctuation, stabilizing *s*-wave pairing. Then in addition, there may be enhancer intraband interactions that are necessarily attractive and peaked around $\tilde{\mathbf{q}} = (0, 0)$ (**Figure 13*c*,*d***). These interactions universally boost pairing irrespective of the underlying gap symmetry and may come from $SrTiO_3$ phonons (6) and/or nematic fluctuations.

Although this pairing framework is appealing owing to its inclusive nature, we emphasize that other than the $SrTiO_3$ phonon mode, there have been no experimental indications of the other interactions shown in **Figure 13**. Some suggest that density functional theory calculations of 1UC FeSe/$SrTiO_3$ with checkerboard antiferromagnetism [$\tilde{\mathbf{q}} = (\pi, \pi)$] best resemble experimental data (67, 111, 112), thus motivating the possible existence of related spin fluctuations. Others take the orbitally ordered state of bulk FeSe as a hint of possible ferro-orbital [nematic, $\tilde{\mathbf{q}} = (0, 0)$] or antiferro-orbital [$\tilde{\mathbf{q}} = (\pi, \pi)$] fluctuations (91, 92).

3.4.1. Pairing involving incipient bands. Alternatively, we recall that inelastic neutron scattering measurements have detected stripe spin fluctuations [$\tilde{\mathbf{q}} = (\pi, 0)$] in bulk FeSe (82–84), similar to many iron pnictide compounds. At first glance, it is unclear whether such interactions, if they persist in 1UC FeSe/$SrTiO_3$, would be useful for pairing. The usual hole pocket at the BZ center, located $\Delta\tilde{\mathbf{k}} = (\pi, 0)$ away from the Fermi electron pockets, is sunken 65–80 meV below the Fermi energy (**Figure 2**). However, ARPES measurements have demonstrated that in LiFeAs, a

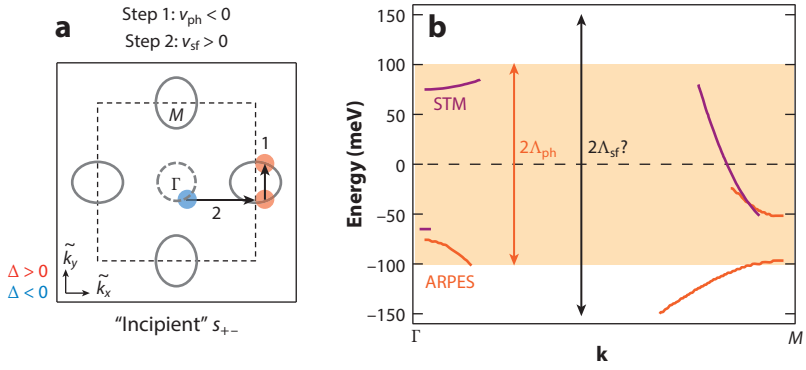

Figure 14

"Bootstrap" mechanism of pairing (107). (*a*) Step 1: An attractive intraband interaction, such as $\tilde{\mathbf{q}} \sim (0, 0)$ coupling to $SrTiO_3$ phonons (ph), opens up a same-sign gap within the Fermi pockets at M. Step 2: A repulsive interband interaction, possibly $\tilde{\mathbf{q}} \sim (\pi, 0)$ spin fluctuations (sf), "bootstraps" to the M pocket gaps and opens up an additional opposite-sign gap on the sunken hole pocket at Γ. Together, the gap function has overall s_{+-} symmetry. (*b*) Band structure diagram informed by scanning tunneling microscopy (STM) (36) and angle-resolved photoemission spectroscopy (ARPES) (6) measurements. The energy scales of phonons and spin fluctuations (interactions v_{ph}, v_{sf} and cutoffs Λ_{ph}, Λ_{sf}), along with the low-lying bands, determine the extent to which "bootstrapping" can enhance T_c.

superconducting gap can develop on a sunken hole pocket 10 meV below the Fermi energy (113). Motivated by this observation, Chen et al. proposed a "bootstrap" mechanism of pairing involving incipient bands in 1UC FeSe/$SrTiO_3$ (107).

The basic picture proposed by Chen et al. is illustrated in **Figure 14*a***. In the weak-coupling limit, interactions such as $\tilde{\mathbf{q}} = (\pi, 0)$ spin fluctuations between a Fermi sheet and an incipient band cannot open up a superconducting gap by themselves. However, if there are preexisting interactions, such as phonons, that stabilize a small gap within the Fermi sheet, then spin fluctuations from incipient bands can come into play and enhance pairing. In 1UC FeSe/$SrTiO_3$, this mechanism results in incipient s_{+-} symmetry, in which the Fermi electron pockets host same-sign gaps and the sunken hole pocket at the zone center hosts an opposite-sign gap. From the author's calculations, incipient bands can boost T_c by an order of magnitude, although numbers are sensitive to estimates of interaction strengths and cutoff.

An appealing feature of this model in the context of 1UC FeSe/$SrTiO_3$ is that the Fermi electron pockets and sunken hole pocket barely or do not overlap in energy (depending on the degree of electron doping). Such a superconducting state would likely be immune to nonmagnetic impurities (114), as elastic scattering would not mix opposite-sign quasiparticles. Indeed, QPI measurements have confirmed that there is no electron-hole pocket scattering near the gap energy (36, 44). Thus, the defect experiments by Fan et al. could also be consistent with incipient s_{+-} gap symmetry.

Recently, Huang et al. uncovered a Γ electron pocket 80 meV above E_F (**Figure 14*b***), using empty-state STM measurements (36). This pocket may be similar to one discovered in K-coated bulk $FeSe_{0.55}Te_{0.45}$ (115) and FeSe (76), or a shallow Z-electron Fermi pocket in 3D $(Tl, Rb)_yFe_{2-x}Se_2$ (116). Given that this pocket lies within the $SrTiO_3$ phonon energy (100 meV), it may be interesting to explore whether it has any positive contribution to T_c in 1UC FeSe/$SrTiO_3$ (117).

4. SUMMARY AND OUTLOOK

In this review, we have surveyed key experimental and theoretical developments related to 1UC FeSe/$SrTiO_3$ from its time of discovery, 2012, to early 2016. The major themes we have presented and developed can be captured in the following five statements:

1. Monolayer FeSe on $SrTiO_3$ exemplifies a dramatic interface effect, in which a UC layer of free-standing FeSe is nonsuperconducting down to 2.2 K but subsequently exhibits T_c ranging from 65 K to 109 K when coupled to $SrTiO_3$.
2. Experiments probing an air-sensitive, monolayer film are demanding in nature, but this challenge motivates the development and use of improved in situ instrumentation, such as four-probe STM, which in turn may lead to discoveries of new systems.
3. Capping of 1UC FeSe/$SrTiO_3$ has not yet been optimized. Not only is it crucial for protecting films from atmospheric exposure but it simultaneously provides a second interface that could yet be engineered to enhance electronic properties.
4. Experiments have uncovered clues of both conventional and unconventional mechanisms of pairing in 1UC FeSe/$SrTiO_3$. Although the ARPES replica bands are best explained by cross-interface coupling to $SrTiO_3$ phonon modes, more experiments verifying their nature and influence on T_c are desirable (118). And although accumulated experience with iron-based superconductors might suggest the importance of spin (and orbital) fluctuations, direct measurements of magnetic excitations in 1UC FeSe/$SrTiO_3$ are still needed.
5. Various pairing scenarios have been proposed in which multiple bosons, such as phonons and spin fluctutations, can work cooperatively in a multiband environment to enhance T_c in 1UC FeSe/$SrTiO_3$. Although these theories still require experimental confirmation, they represent an appealing "best-of-both-worlds" approach to finding and creating superconductors with even higher T_c. Combined with the layered 2D architecture of 1UC FeSe/$SrTiO_3$ in which these cooperative effects may be realized and engineered, many possibilities abound down the road.

DISCLOSURE STATEMENT

The authors are not aware of any affiliations, memberships, funding, or financial holdings that might be perceived as affecting the objectivity of this review.

ACKNOWLEDGMENTS

The authors would like to thank C.-Z. Chang, S. Coh, S. Fang, J.-F. Ge, P.J. Hirschfeld, E. Kaxiras, S.A. Kivelson, D.-H. Lee, I.I. Mazin, Z.-X. Shen, C.-L. Song, T.A. Webb, and K. Zou for valuable discussions that have informed many of the views and ideas presented in this review. Our work on 1UC FeSe/$SrTiO_3$ was supported by the National Science Foundation under Grants No. DMR-0847433 and No. PHY-1231319 (Science and Technology Center at the Center for Integrated Quantum Materials), and the Gordon and Betty Moore Foundation's Emergent Phenomena in Quantum Systems Initiative through Grant. No. GBMF4536. J.E. Hoffman acknowledges support from the Canadian Institute for Advanced Research.

LITERATURE CITED

1. Reyren N, Thiel S, Caviglia AD, Kourkoutis LF, Hammerl G, et al. 2007. *Science* 317:1196–99
2. Gozar A, Logvenov G, Fitting Kourkoutis L, Bollinger AT, Giannuzzi LA, et al. 2008. *Nature* 455:782–85
3. Wang QY, Li Z, Zhang WH, Zhang ZC, Zhang JS, et al. 2012. *Chin. Phys. Lett.* 29:037402

4. He S, He J, Zhang W, Zhao L, Liu D, et al. 2013. *Nat. Mater.* 12:605–10
5. Tan S, Zhang Y, Xia M, Ye Z, Chen F, et al. 2013. *Nat. Mater.* 12:634–40
6. Lee JJ, Schmitt FT, Moore RG, Johnston S, Cui YT, et al. 2014. *Nature* 515:245–48
7. Zhang Z, Wang YH, Song Q, Liu C, Peng R, et al. 2015. *Sci. Bull.* 60:1301–4
8. Ge JF, Liu ZL, Liu C, Gao CL, Qian D, et al. 2015. *Nat. Mater.* 14:285–89
9. Hsu FC, Luo JY, Yeh KW, Chen TK, Huang TW, et al. 2008. *PNAS* 105:14262–64
10. Okamoto H. 1991. *J. Phase Equilib.* 12:383–89
11. Song CL, Wang YL, Cheng P, Jiang YP, Li W, et al. 2011. *Science* 332:1410–13
12. Song CL, Wang YL, Jiang YP, Li Z, Wang L, et al. 2011. *Phys. Rev. B* 84:020503
13. Simonin J. 1986. *Phys. Rev. B* 33:7830–32
14. Böhmer AE, Hardy F, Eilers F, Ernst D, Adelmann P, et al. 2013. *Phys. Rev. B* 87:180505
15. Schmidbauer M, Kwasniewski A, Schwarzkopf J. 2012. *Acta. Crystallogr. B* 68:8–14
16. Zhang T, Cheng P, Li WJ, Sun YJ, Wang G, et al. 2010. *Nat. Phys.* 6:104–8
17. Liu D, Zhang W, Mou D, He J, Ou YB, et al. 2012. *Nat. Commun.* 3:931
18. Shimojima T, Suzuki Y, Sonobe T, Nakamura A, Sakano M, et al. 2014. *Phys. Rev. B* 90:121111
19. Nakayama K, Miyata Y, Phan GN, Sato T, Tanabe Y, et al. 2014. *Phys. Rev. Lett.* 113:237001
20. Watson MD, Kim TK, Haghighirad AA, Davies NR, McCollam A, et al. 2015. *Phys. Rev. B* 91:155106
21. Zhang P, Qian T, Richard P, Wang XP, Miao H, et al. 2015. *Phys. Rev. B* 91:214503
22. Peng R, Xu HC, Tan SY, Cao HY, Xia M, et al. 2014. *Nat. Commun* 5:5044
23. Zhang W, Li Z, Li F, Zhang H, Peng J, et al. 2014. *Phys. Rev. B* 89:060506
24. Peng R, Shen XP, Xie X, Xu HC, Tan SY, et al. 2014. *Phys. Rev. Lett.* 112:107001
25. Zhang WH, Sun Y, Zhang JS, Li FS, Guo MH, et al. 2014. *Chin. Phys. Lett.* 31:017401
26. Deng LZ, Lv B, Wu Z, Xue YY, Zhang WH, et al. 2014. *Phys. Rev. B* 90:214513
27. Sun Y, Zhang W, Xing Y, Li F, Zhao Y, et al. 2014. *Sci. Rep.* 4:6040
28. Cui YT, Moore RG, Zhang AM, Tian Y, Lee JJ, et al. 2015. *Phys. Rev. Lett.* 114:037002
29. Tian YC, Zhang WH, Li FS, Wu YL, Wu Q, et al. 2016. *Phys. Rev. Lett.* 116:107001
30. Li F, Ding H, Tang C, Peng J, Zhang Q, et al. 2015. *Phys. Rev. B* 91:220503
31. Zhao W, Zhang CZ, Jiang J, Moodera J, Chan M. 2016. *Bull. Am. Phys. Soc.* 61:B11.00011
32. Zhu Y, Tsai CF, Wang H. 2013. *Supercond. Sci. Technol.* 26:025009
33. Bozovic I, Ahn C. 2014. *Nat. Phys.* 10:892–95
34. Božović I. 2016. *Nat. Phys.* 12:22–24
35. Lin Y, Becerra-Toledo AE, Silly F, Poeppelmeier KR, Castell MR, Marks LD. 2011. *Surf. Sci.* 605:L51–55
36. Huang D, Song CL, Webb TA, Fang S, Chang CZ, et al. 2015. *Phys. Rev. Lett.* 115:017002
37. Bang J, Li Z, Sun YY, Samanta A, Zhang YY, et al. 2013. *Phys. Rev. B* 87:220503
38. Kawasaki M, Takahashi K, Maeda T, Tsuchiya R, Shinohara M, et al. 1994. *Science* 266:1540–42
39. Ohnishi T, Shibuya K, Lippmaa M, Kobayashi D, Kumigashira H, et al. 2004. *Appl. Phys. Lett.* 85:272–74
40. Connell JG, Isaac BJ, Ekanayake GB, Strachan DR, Seo SSA. 2012. *Appl. Phys. Lett.* 101:251607
41. Berlijn T, Cheng HP, Hirschfeld PJ, Ku W. 2014. *Phys. Rev. B* 89:020501
42. Li F, Zhang Q, Tang C, Liu C, Shi J, et al. 2016. *2D Mater.* 3:024002
43. Li Z, Peng JP, Zhang HM, Zhang WH, Ding H, et al. 2014. *J. Phys. Condens. Matter* 26:265002
44. Fan Q, Zhang WH, Liu X, Yan YJ, Ren MQ, et al. 2015. *Nat. Phys.* 11:946–52
45. Li N, Li Z, Ding H, Ji S, Chen X, Xue QK. 2013. *Appl. Phys. Exp.* 6:113101
46. Moore R. 2015. *Bull. Am. Phys. Soc.* 60:Z51.00001
47. Zhou G, Zhang D, Liu C, Tang C, Wang X, et al. 2016. *Appl. Phys. Lett.* 108:202603
48. Zhang P, Peng XL, Qian T, Richard P, Shi X, et al. 2016. *Phys. Rev. B* 94:104510
49. Ding H, Lv YF, Zhao K, Wang WL, Wang L, et al. 2016. *Phys. Rev. Lett.* 117:067001
50. Rebec S, Jia T, Zhang C, Hashimoto M, Lu D, et al. 2016. arXiv:1606.09358
51. Zou K, Mandal S, Albright SD, Peng R, Pu Y, et al. 2016. *Phys. Rev. B* 93:180506
52. Erdman N, Poeppelmeier KR, Asta M, Warschkow O, Ellis DE, Marks LD. 2002. *Nature* 419:55–58
53. Herger R, Willmott PR, Bunk O, Schlepütz CM, Patterson BD, Delley B. 2007. *Phys. Rev. Lett.* 98:076102
54. Huang D, Webb TA, Fang S, Song CL, Chang CZ, et al. 2016. *Phys. Rev. B* 93:125129
55. Drozdov AP, Eremets MI, Troyan IA, Ksenofontov V, Shylin SI. 2015. *Nature* 525:73–76

56. Gao L, Xue YY, Chen F, Xiong Q, Meng RL, et al. 1994. *Phys. Rev. B* 50:4260–63
57. Mazin II, Singh DJ, Johannes MD, Du MH. 2008. *Phys. Rev. Lett.* 101:057003
58. Kuroki K, Onari S, Arita R, Usui H, Tanaka Y, et al. 2008. *Phys. Rev. Lett.* 101:087004
59. Boeri L, Dolgov OV, Golubov AA. 2008. *Phys. Rev. Lett.* 101:026403
60. Onari S, Kontani H. 2009. *Phys. Rev. Lett.* 103:177001
61. Choudhury N, Walter EJ, Kolesnikov AI, Loong CK. 2008. *Phys. Rev. B* 77:134111
62. Xie Y, Cao HY, Zhou Y, Chen S, Xiang H, Gong XG. 2015. *Sci. Rep.* 5:10011
63. Wang Z, McKeown Walker S, Tamai A, Wang Y, Ristic Z, et al. 2016. *Nat. Mater.* 3:1–6
64. Lee DH. 2015. *Chin. Phys. B* 24:117405
65. Rademaker L, Wang Y, Berlijn T, Johnston S. 2016. *New J. Phys.* 18:022001
66. Mazin II. 2015. *Nat. Mater.* 14:755–56
67. Coh S, Cohen ML, Louie SG. 2015. *New J. Phys.* 17:073027
68. Tang C, Liu C, Zhou G, Li F, Ding H, et al. 2016. *Phys. Rev. B* 93:020507
69. Chen W, Zeng C, Kaxiras E, Zhang Z. 2016. *Phys. Rev. B* 93:064517
70. Lu XF, Wang NZ, Wu H, Wu YP, Zhao D, et al. 2015. *Nat. Mater.* 14:325–29
71. Zhao L, Liang A, Yuan D, Hu Y, Liu D, et al. 2016. *Nat. Commun.* 7:10608
72. Niu XH, Peng R, Xu HC, Yan YJ, Jiang J, et al. 2015. *Phys. Rev. B* 92:060504
73. Du Z, Yang X, Lin H, Fang D, Du G, et al. 2016. *Nat. Commun.* 7:10565
74. Yan YJ, Zhang WH, Ren MQ, Liu X, Lu XF, et al. 2016. *Phys Rev. B* 94:134502
75. Miyata Y, Nakayama K, Sugawara K, Sato T, Takahashi T. 2015. *Nat. Mater.* 14:775–79
76. Wen CHP, Xu HC, Chen C, Huang ZC, Lou X, et al. 2016. *Nat. Commun.* 7:10840
77. Ye ZR, Zhang CF, Ning HL, Li W, Chen L, et al. 2015. arXiv:1512.02526
78. Tang C, Zhang D, Zang Y, Liu C, Zhou G, et al. 2015. *Phys. Rev. B* 92:180507
79. Zhang WH, Liu X, Wen CHP, Peng R, Tan SY, et al. 2016. *Nano Lett.* 16:1969–73
80. Song CL, Zhang HM, Zhong Y, Hu XP, Ji SH, et al. 2016. *Phys. Rev. Lett.* 116:157001
81. Wen CHP, Xu HC, Chen C, Huang ZC, Lou X, et al. 2016. *Nat. Commun.* 7:10840
82. Rahn MC, Ewings RA, Sedlmaier SJ, Clarke SJ, Boothroyd AT. 2015. *Phys. Rev. B* 91:180501
83. Wang Q, Shen Y, Pan B, Hao Y, Ma M, et al. 2016. *Nat. Mater.* 15:159–63
84. Wang Q, Shen Y, Pan B, Zhang X, Ikeuchi K, et al. 2016. *Nat. Commun.* 7:12182
85. McQueen TM, Williams AJ, Stephens PW, Tao J, Zhu Y, et al. 2009. *Phys. Rev. Lett.* 103:057002
86. Zhang Y, Yi M, Liu ZK, Li W, Lee JJ, et al. 2016. 94:115153
87. Medvedev S, McQueen TM, Troyan IA, Palasyuk T, Eremets MI, et al. 2009. *Nat. Mater.* 8:630–33
88. Fernandes RM, Schmalian J. 2012. *Supercond. Sci. Technol.* 25:084005
89. Yamase H, Zeyher R. 2013. *Phys. Rev. B* 88:180502
90. Lederer S, Schattner Y, Berg E, Kivelson SA. 2015. *Phys. Rev. Lett.* 114:097001
91. Dumitrescu PT, Serbyn M, Scalettar RT, Vishwanath A. 2016. *Phys Rev. B* 94:155127
92. Li ZX, Wang F, Yao H, Lee DH. 2016. *Sci. Bull.* 61:925–30
93. Kang J, Fernandes RM. 2016. arXiv:1606.01170
94. Linscheid A, Maiti S, Wang Y, Johnston S, Hirschfeld PJ. 2016. *Phys. Rev. Lett.* 117:077003
95. Glasbrenner JK, Mazin II, Jeschke HO, Hirschfeld PJ, Fernandes RM, Valentí R. 2015. *Nat. Phys.* 11:953–58
96. Wang F, Kivelson SA, Lee DH. 2015. *Nat. Phys.* 11:959–63
97. Chubukov AV, Fernandes RM, Schmalian J. 2015. *Phys. Rev. B* 91:201105
98. Yu R, Si Q. 2015. *Phys. Rev. Lett.* 115:116401
99. Gastiasoro MN, Eremin I, Fernandes RM, Andersen BM. 2016. arXiv:1607.04711
100. Tafti FF, Juneau-Fecteau A, Delage ME, René de Cotret S, Reid JP, et al. 2013. *Nat. Phys.* 9:349–52
101. Hirschfeld PJ, Korshunov MM, Mazin II. 2011. *Rep. Prog. Phys.* 74:124508
102. Wollman DA, Van Harlingen DJ, Lee WC, Ginsberg DM, Leggett AJ. 1993. *Phys. Rev. Lett.* 71:2134–37
103. Hirschfeld PJ, Altenfeld D, Eremin I, Mazin II. 2015. *Phys. Rev. B* 92:184513
104. Mazin II. 2011. *Phys. Rev. B* 84:024529
105. Maier TA, Graser S, Hirschfeld PJ, Scalapino DJ. 2011. *Phys. Rev. B* 83:100515
106. Kreisel A, Wang Y, Maier TA, Hirschfeld PJ, Scalapino DJ. 2013. *Phys. Rev. B* 88:094522
107. Chen X, Maiti S, Linscheid A, Hirschfeld PJ. 2015. *Phys. Rev. B* 92:224514

108. Zhang Y, Lee JJ, Moore RG, Li W, Yi M, et al. 2016. *Phys. Rev. Lett.* 117:117001
109. Beaird R, Vekhter I, Zhu JX. 2012. *Phys. Rev. B* 86:140507
110. Xiang YY, Wang F, Wang D, Wang QH, Lee DH. 2012. *Phys. Rev. B* 86:134508
111. Bazhirov T, Cohen ML. 2013. *J. Phys. Condens. Matter* 25:105506
112. Zheng F, Wang Z, Kang W, Zhang P. 2013. *Sci. Rep.* 3:2213
113. Miao H, Qian T, Shi X, Richard P, Kim TK, et al. 2015. *Nat. Commun.* 6:6056
114. Chen X, Mishra V, Maiti S, Hirschfeld PJ. 2016. *Phys. Rev. B* 94:054524
115. Zhang P, Richard P, Xu N, Xu YM, Ma J, et al. 2014. *Appl. Phys. Lett.* 105:172601
116. Liu ZH, Richard P, Xu N, Xu G, Li Y, et al. 2012. *Phys. Rev. Lett.* 109:037003
117. Shi X, Han ZQ, Peng XL, Richard P, Qian T, et al. 2016. arXiv:1606.01470
118. Zhang S, Guan J, Jia X, Liu B, Wang W, et al. 2016. *Phys. Rev. B* 94:081116R